

BOSONIC POLARON IN A ^{39}K BEC

BOSONISK POLARON I ET ^{39}K BEC

The University of Aarhus
Faculty of Science
Department of Physics and Astronomy

Master of Science Thesis

Kristoffer Theis Skalmstang
Supervisor: Jan Arlt
July 2015

ABSTRACT

Ultracold gases provide a versatile system to investigate fundamental properties of atomic and molecular interactions. Since the first realization of a Bose-Einstein Condensate (BEC) in 1995 by E. Cornell and C. Wieman [1] this field has made dramatic progress [2–4]. In particular the identification of Feshbach resonances (FR) has led to a new level of controllability of the atom interactions [5]. This has for example made the realization of a dual species ^{87}Rb and ^{39}K BEC possible in our lab [6]. These FR has recently been applied in the discovery of the Fermi polaron in an ultracold Fermi sea. The properties of this quasiparticle, composed of the an impurity and its surrounding medium, gives fundamental insight in systems, such as an electron moving in polarizable medium, but has yet to be realized in an ultracold bosonic medium.

In the scope of this thesis the first fundamental study of the Bose polaron in an ultracold gas was achieved [7]. By utilizing an interstate Feshbach resonance between two internal spin states of ^{39}K and performing radio frequency spectroscopy between these spin states, the energy of the Bose polaron was mapped out experimentally. A variational theory, using a truncated basis method (TBM) including three-body correlations, fully reproduces the rich polaron spectrum obtained experimentally. In particular the theoretical result produced with this method agrees within one standard deviation, for the region stretching from the attractive side of the FR far into the region, shared by the polaron branches and the molecular band. For the fully repulsive polaron branch the theory breaks down, because lower lying energy states allow for decay of the repulsive polaron, leading to strong dependence on higher order coupling that the theory does not take into account.

CONTENTS

1	Introduction	1
2	Theoretical background	3
2.1	Bose-Einstein Condensate	3
2.2	Feshbach Resonances	4
2.3	Bose Polaron	6
2.4	Beyond Fröhlich polarons	8
3	Experimental Apparatus	11
3.1	Experimental overview	11
3.2	Laser systems	12
3.2.1	Rb laser system	13
3.2.2	K laser system	15
3.2.3	Laser characterization	16
3.3	Magneto-Optical Trap	20
3.4	Magnetic Trap and field control	23
3.4.1	MOT and Transport coils	23
3.4.2	Magnetic Trap	23
3.4.3	Evaporative cooling	25
3.4.4	Magnetic field compensation	25
3.5	Optical dipole trap	26
3.6	State preparation	29
3.7	Absorption imaging	30
3.8	Dual species BEC	31
4	Measuring the Bose polaron	33
4.1	Magnetic field calibration	35
4.2	Characterizing the inter-state Feshbach Resonance	36
4.3	Polaron spectroscopy	39
4.3.1	Energy spectrum	41

4.3.2	Energy	42
4.3.3	Energy width	42
4.3.4	Power dependence	43
4.3.5	Concentration dependence	43
5	Conclusion and Outlook	49
A	Poster	I

Introduction

When a particle is immersed into a foreign medium, the presence of an interaction between this impurity and its surroundings can lead to the formation of quasiparticles, termed polarons, with different properties from that of the free particle. Since Landau and Pekar first described this mechanism in 1933 [8], when studying an electron moving through a polarizable medium, it has been of fundamental interest to characterize these quasiparticles as they are a keystone in understanding many problems of higher complexity. In this classic example of the electron moving in solid state, the lattice displacements described as a phonon bath and the coulomb interaction, lead to a dressing of the electron and phonon energies. Their composition acts as a new particle, the polaron, with a new distinct energy spectrum. These systems have already been studied extensively in solid physics, but practical limitations such as the purity of the medium and control of the interaction strength limit the experiments.

Ultracold quantum gases are a system with high degree of control and purity. Specifically the identification of magnetically tunable Feshbach resonances (FR) has led to the possibility to study the polaron at a wide range of interaction strengths. Besides this the flexibility of the trap construction makes it possible to study more exotic configurations and dynamics in comparison with solid state systems, where the dimensions are fixed.

Fermionic systems with such polarons have already been realized [2–4], but prior to this work, the canonical study of an impurity in a bosonic gas had not yet been achieved. This investigation is important for the understanding of the aforementioned solid state system and could even give insight as of how the elementary particles accumulate mass by interaction with the Higgs boson.

For the Fermi polaron, the investigation is conventionally done by preparing a majority and a minority component that are internally and mutually weakly interacting. Conveniently the impurity and medium atoms can be chosen as different species of fermionic atoms. The latter forms the impurities as it is transformed into a state, which is strongly interacting with the majority component. Typically this is done with radio frequency (RF) spectroscopy and as a result the polaron state is probed.

This technique could straightforwardly be extended and applied to impurities in a bosonic medium. However, we use two internal spin states of ^{39}K as medium and impurity, and opposed to previous work, we form the polaron directly from the medium. A single condensate is prepared and a RF pulse spin flip part of the condensate into a state, which interacts strongly with the remaining condensate through a FR. By performing spectroscopy the loss of atoms in the BEC provide a signal which is used to characterize the polaron for all interactions.

The thesis is structured as follows:

- In chapter 2 the theoretical background of ultracold gases and their interactions are briefly reviewed. This includes the formation of a BEC, a description of Feshbach resonances and the properties of the polaron.
- Chapter 3 Describes a generic experimental apparatus for creation of dual species BECs.
- In chapter 4 a description of the experimental procedure for observing the polaron is given, and the main results are presented, along with supplementary measurements.
- A conclusion and an overview of my involvement is finally given in chapter 5, along with an outlook.

Theoretical background

Three major parts are necessary to understand the investigation of polarons in ultracold gases. First of all the formation of the BEC used to achieve the high density for the medium, which makes the strongly interacting regime available. This is described in section 2.1. Secondly the scattering between atoms and the phenomenon of FRs is described in section 2.2. This is important as it facilitates the tuning of the interactions in the system explored. Lastly the features of the polaron is explained in section 2.3, as the model of the system developed by our collaborators in [7] is presented.

2.1 Bose-Einstein Condensate

For temperatures T well above absolute zero, the bosonic spin one particles with mass m are well described by the Maxwell-Boltzmann distribution. Here the average number of particles n of the i -th energy level ϵ_i is given by:

$$n(\epsilon_i) = \frac{1}{e^{(\epsilon_i - \mu)/k_B T}},$$

where k_B is the Boltzmann constant. μ is the chemical potential assumed to be well below the particle energy spacings. As the temperature of the gas is lowered the particle's quantum statistics becomes relevant. This happens when the de Broglie wavelength

$$\lambda_{dB} = \frac{2\pi\hbar}{\sqrt{3mk_B T}},$$

becomes comparable with the inter-particle spacing, at which point the single particle wave functions overlap and become indistinguishable. As this limit is reached the ground state of the system will become macroscopically occupied by one coherent wave function, known as the Bose-Einstein Condensate. At absolute zero all the particles can be described by one ground state wave function, but this is unreachable due to the Heisenberg limit. Typically the cloud is trapped in a harmonic oscillator where the inter-particle distance and the lowest energy level is

related to the trapping frequencies ω , therefore another way of stating the limit of a BEC is given by the phase-space density (PSD)[9]:

$$\rho = \frac{N}{V} \lambda_{dB}^3 = n \left(\frac{2\pi\hbar^2}{mk_B T} \right)^{3/2} \leq 1.202,$$

where N is the total number of atoms and V is the volume.

Whereas quantum statistics gives the PSD limit for condensation to a BEC, it does not describe the BEC wave function. This however arises as a solution to the Gross-Pitaevskii equation (GPE):

$$\mu\psi(\mathbf{r}) = \left(-\frac{\hbar^2}{2m} \nabla^2 + U(\mathbf{r}) + g|\psi(\mathbf{r})|^2 \right) \psi(\mathbf{r}),$$

where g is the scattering parameter, $U(\mathbf{r})$ is the spacial dependent potential, which for a harmonic trap is given by $U(\mathbf{r}) = \frac{1}{2}m(\omega_x^2 r_x^2 + \omega_y^2 r_y^2 + \omega_z^2 r_z^2)$. This macroscopic model is similar to the Schrödinger equation but takes into account the scattering in between the particles by the additional third term.

For the ultracold gases it is for most cases safe to make the Thomas-Fermi approximation which neglects the kinetic energy (first term in GPE). By doing so the density throughout the cloud can easily be determined:

$$n(\mathbf{r}) = \frac{\mu - V(\mathbf{r})}{g}.$$

Which will result in a parabolic distribution for a harmonic trap, for a pure BEC. If a part of the cloud has not been condensed the distribution will be bimodal with respect to both the parabolic BEC distribution and a Gaussian thermal cloud distribution.

2.2 Feshbach Resonances

The low energy elastic scattering in ultracold gases is mainly governed by s-wave scattering. For this we introduce the s-wave scattering length a , which one can think of as the distance over which interaction occurs. This is related to the scattering cross-section (that many seem more familiar with) in the following way:

$$\sigma = 4\pi a^2.$$

For two-body elastic scattering processes there will be a phase shift between the incoming and outgoing wave function related to the scattering length

$$\tan(\phi_0) = -ka.$$

For a collision with small incoming energy E , the scattering process will be represented by a energetically open channel potential, see potential in figure 2.1a. If a second potential that allows for a bound molecular (or dimer) state is present, represented by the closed channel in figure 2.1a, the phase shift will be strongly altered, if the energy of this bound molecular state E_c matches that of the incoming energy. This leads to a diverging scattering length that can be both positive, referred to as repulsive, for $E_c < E$, and negative, referred to as attractive, for $E_c > E$.

The closed channels arise from excited atomic states and some of these can be altered relative to each other since their respective energies can depend either the magnetic Zeeman effect or the Stark effect. These are referred to as the magnetically tunable and optically tunable FR, respectively. For small scattering lengths the magnetically tunable FR's dependence on the B -field can be approximated by [5]

$$a(B) = a_{bg} \left(1 - \frac{\Delta}{B - B_0} \right),$$

where a_{bg} is the background scattering length, B_0 is the FR position, Δ is the resonance width. An example of such magnetically tunable FRs is shown in figure 2.1b along with the the associated bound state molecular energy in figure 2.1c. For the small scattering lengths the molecular binding energy is given by

$$E_b = \frac{\hbar^2}{4mR^{*2}} \left(\sqrt{1 + \frac{4R^*}{a}} - 1 \right)^2, \quad (2.2.1)$$

where $R^* = \frac{\hbar^2}{ma_{bg}\delta\mu\Delta}$ is the range parameter, $\delta\mu$ denotes the difference in magnetic moment of the open and closed channel. This is utilized to characterize the FR in section 4.2.

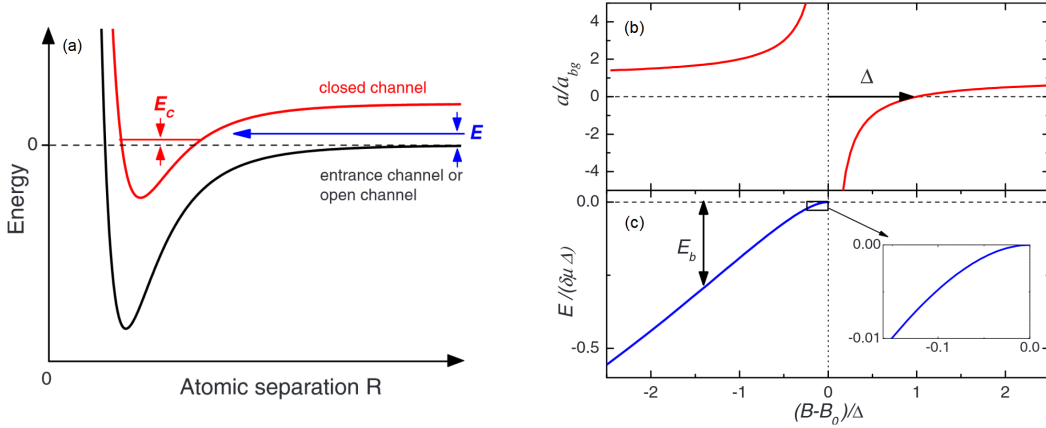


Figure 2.1: Physical features of a Feshbach Resonance. (a) shows the scattering process leading to a FR. An atom entering the open channel potential (black solid line) with energy E (blue arrow). The presence of a molecular energy level E_c due to a closed channel potential (red solid line) strongly alters the phase shift ϕ_0 during the scattering process. (b) The scattering length plotted against B -field (red solid line) is characterized by the width of the resonance Δ , along with the resonance position B_0 and the background scattering length a_{bg} . The molecular channel (c) leads to a bound state (blue solid line). Figure reproduced from [10].

2.3 Bose Polaron

The theoretical model describes the interaction between a minority impurity and the medium atoms. To make high interaction strengths available the medium is assumed to be a Bose-Einstein condensate, since the probability of scattering scales with density. Since the BEC forms the medium, this will interchangeably be referred to as the Bose atoms or BEC, throughout the thesis. Assuming that the BEC is internally weakly interacting, this type of system can be described by microscopical Bogoliubov theory with the following Hamiltonian [11]:

$$\begin{aligned}
 H = & \sum_{\mathbf{k}} \epsilon_{\mathbf{k}}^B a_{\mathbf{k}}^\dagger a_{\mathbf{k}} + \frac{1}{2V} \sum_{\mathbf{k}, \mathbf{p}, \mathbf{q}} g_B(\mathbf{q}) a_{\mathbf{k}+\mathbf{q}}^\dagger a_{\mathbf{p}-\mathbf{q}}^\dagger a_{\mathbf{p}} a_{\mathbf{k}} \\
 & + \sum_{\mathbf{p}} \epsilon_{\mathbf{p}} c_{\mathbf{p}}^\dagger c_{\mathbf{p}} + \frac{1}{V} \sum_{\mathbf{k}, \mathbf{p}, \mathbf{q}} g_I(\mathbf{q}) c_{\mathbf{k}+\mathbf{q}}^\dagger a_{\mathbf{p}-\mathbf{q}}^\dagger a_{\mathbf{p}} c_{\mathbf{k}}, \quad (2.3.1)
 \end{aligned}$$

where $a_{\mathbf{k}}^{(\dagger)}$ and $c_{\mathbf{k}}^{(\dagger)}$ removes (adds) a boson and an impurity with momentum \mathbf{k} , respectively. The kinetic energy of the impurity (medium) atoms is $\epsilon_{\mathbf{k}}^{(B)} = \frac{\hbar^2 k^2}{2m^{(B)}}$ and for this experiment their kinetic energies are the same since the mass $m^{(B)}$ of both are that of ^{39}K , m_K . The interaction parameters g_B , for the interaction between bosons, and g_I , for the interaction between the impurities and bosons, are approximated by s-wave scattering and have the following relation to the scattering

length

$$g = \frac{4\pi\hbar^2 a}{m_K}.$$

The first term in eq. (2.3.1) describes the kinetic energy of the Bosonic particles in the cloud. The second term describes the scattering between two bosonic atoms and the transfer of a momentum \mathbf{q} from one atom to another. The factor $1/2$ in front of this term is the symmetry factor, compensating for counting the bosons twice. The third term describes the impurity atoms kinetic energy. The fourth term describe the scattering between the impurity atoms and the medium atoms. A fifth term of the impurity atoms scattering on themselves are also possible, but has been neglected since it is assumed that the concentration of impurities is low enough that they mainly scatter on the bosons rather than each other. Note that this neglect of the fifth term makes the theory generic for both a fermionic and a bosonic impurity.

Performing the Bogoliubov transformation with $a_{\mathbf{k}} = u_{\mathbf{k}}\alpha_{\mathbf{k}} - v_{\mathbf{k}}\alpha_{-\mathbf{k}}^\dagger$, with real and positive coherence factors $v_{\mathbf{k}}^2 = \frac{1}{2}\left(\frac{\epsilon_{\mathbf{k}}^B + n_B g_B}{\gamma_{\mathbf{k}}} - 1\right)$ and $u_{\mathbf{k}}^2 = \frac{1}{2}\left(\frac{\epsilon_{\mathbf{k}}^B + n_B g_B}{\gamma_{\mathbf{k}}} + 1\right)$ on eq. (2.3.1) yields

$$\begin{aligned} H &= H_0 + H_{IB} \\ H_0 &= E_g + \sum_{\mathbf{k}} \gamma_{\mathbf{k}} \alpha_{\mathbf{k}}^\dagger \alpha_{\mathbf{k}} + \sum_{\mathbf{p}} \epsilon_{\mathbf{p}} c_{\mathbf{p}}^\dagger c_{\mathbf{p}} \\ H_{IB} &= \frac{1}{V} \left(N_B g_I(0) \sum_{\mathbf{p}} c_{\mathbf{p}}^\dagger c_{\mathbf{p}} \right. \\ &\quad + \sqrt{N_B} \sum_{\mathbf{p}, \mathbf{q} \neq 0} \sqrt{\frac{\epsilon_{\mathbf{q}}}{\gamma_{\mathbf{q}}}} g_I(\mathbf{q}) c_{\mathbf{p}}^\dagger c_{\mathbf{p}+\mathbf{q}} (\alpha_{\mathbf{q}}^\dagger + \alpha_{-\mathbf{q}}) \\ &\quad \left. + \sum_{\mathbf{p}, \mathbf{q} \neq \mathbf{k}, \mathbf{k} \neq 0} g_I(\mathbf{q}) c_{\mathbf{p}}^\dagger c_{\mathbf{p}+\mathbf{q}} \left((u_{\mathbf{k}+\mathbf{q}} \alpha_{\mathbf{k}+\mathbf{q}}^\dagger - v_{\mathbf{k}+\mathbf{q}} \alpha_{-(\mathbf{k}+\mathbf{q})}) (u_{\mathbf{k}} \alpha_{\mathbf{k}} - v_{\mathbf{k}} \alpha_{-\mathbf{k}}^\dagger) \right) \right), \end{aligned} \quad (2.3.2)$$

where α^\dagger and α are the Bogoliubov phonon creation and annihilation operators, $\gamma_{\mathbf{k}} = \sqrt{\epsilon_{\mathbf{k}}^B (\epsilon_{\mathbf{k}}^B + 2g_B n_B)}$ is the dispersion of the collective Bogoliubov modes, N_B is the number of BEC atoms and n_B is the average density of the BEC. Here E_g is the ground state energy of the non-interacting BEC,

$$E_g = \frac{1}{2} N_B n_B g_B(0) + \frac{1}{2} \sum_{\mathbf{k}} (\gamma_{\mathbf{k}} - \epsilon_{\mathbf{k}}).$$

The first term in H_{IB} leads to the the mean-field shift from the bosons, also known from the Gross-Pitaevskii equation, on the impurities

$$E_{MF} = \frac{4\pi\hbar^2 n_B a}{m_K}.$$

It is convenient to use the inverse interaction parameter $\frac{1}{k_n a}$, where $k_n = (6\pi^2 n_B)^{1/3}$, and the energy scale $E_n \equiv \frac{\hbar^2 k_n^2}{2m_K}$, such that the mean-field shift becomes

$$E_{MF} = \frac{4}{3\pi} \left(\frac{1}{k_n a} \right)^{-1} E_n$$

Note that the interaction parameter goes from large values at low interaction to zero at infinite interaction. These scales will be used extensively in chapter 4.

The treatment of polarons has conventionally been done with departure in the Hamiltonian suggested by Fröhlich, which corresponds to eq. (2.3.2) without the third term in H_{IB} . This takes into account the mean-field shift and the scattering between the impurities and phonons, characterized by the second term, but neglects the second order scattering on the phonon modes, described by the third term. These become important in the strongly interacting regime $\left| \frac{1}{k_n a} \right| \leq 1$, and neglecting this already misses terms on the third order in perturbation theory [11] and variational theory [12].

2.4 Beyond Fröhlich polarons

The inclusion of the third term in H_{IB} has been approached by both a perturbational and variational method.

Perturbation Theory

The Hamiltonian has been evaluated in perturbation, expanding the scattering matrices with all possible pair propagators and then evaluating the corresponding diagram by applying imaginary time Bose Green's functions. For the evaluation to third order in the pair propagators, with zero temperature approximation and for equal mass, the energy shift becomes the following [11],

$$\frac{\Delta E}{E_{MF}} = \frac{a}{\xi} + 8 \frac{\sqrt{2}}{3\pi} \frac{a^2}{\xi^2} + \left(\frac{2}{3} - \frac{\sqrt{3}}{\pi} \right) \frac{a^3}{\xi^3} \ln \left(\frac{a^*}{\xi} \right)$$

. Here \hbar and k_B have been set to one. The healing length of the BEC is $\xi = \frac{1}{\sqrt{8\pi n_B a_B}}$ and $a^* \equiv \max(a, a_B)$.

Another feature describing the system is the quasiparticle residue Z . This expresses whether the impurity wave function is best described as a free particle, when $Z = 0$, or whether it is best described purely by the polaron part, when $Z = 1$. For this theory the quasiparticle residue to third order is given by [11]

$$Z^{-1} = 1 + 2\sqrt{\frac{2}{3}} \frac{a^2}{a_B \xi} + 0.64 \frac{a^3}{a_B \xi^2}$$

This will become important as it perturbs the Rabi frequency of the transition. $\Omega \simeq \sqrt{Z} \Omega_0$. Where Ω_0 is the unperturbed Rabi frequency [2].

Variational method

It turns out that the scattering process between the impurities and the bosons can be treated microscopically as a closed channel dimer formation. This dimer state can be represented by the creation and annihilation operators $d_{\mathbf{k}}^\dagger$ and $d_{\mathbf{k}}$, respectively. The creation operator $d_{\mathbf{k}}^\dagger$ includes the creation of an impurity and a boson atom in the bound dimer state with single particle energy $\epsilon_{\mathbf{k}} = \frac{\epsilon_{\mathbf{k}}}{2}$. This leads to the Hamiltonian stated in [12]

$$\begin{aligned} H &= H_0 + H_{0M} + H_M \\ H_{0M} &= \sum_{\mathbf{k}} (\epsilon_{\mathbf{k}}^d + \nu_0) d_{\mathbf{k}}^\dagger d_{\mathbf{k}} \\ H_M &= g_I \sqrt{n_B} \sum_{\mathbf{p}} (d_{\mathbf{p}}^\dagger c_{\mathbf{p}} + h.c.) + g_I \sum_{\mathbf{p}, \mathbf{q}} (d_{\mathbf{q}}^\dagger c_{\mathbf{q}-\mathbf{p}} a_{\mathbf{p}} + h.c.), \end{aligned} \quad (2.4.1)$$

. This is not obviously equivalent to eq. (2.3.1), but actually is and leads to the exact same physics as the perturbation theory, if taken to infinite order. Here ν_0 is the detuning from the bare atomic transition of the unperturbed impurity and H_{0M} describes the energy associated with the molecule. The third term H_M describes the creation of molecules by annihilation of an impurity and a boson (note that in the Bogoliubov approximation $\sqrt{n_B} \propto \sqrt{\sum_{\mathbf{p}} b_{\mathbf{p}}^\dagger b_{\mathbf{p}}} \simeq \sum_{\mathbf{p}} b_{\mathbf{p}}$), or opposite for the hermitian conjugate (*h.c.*). This dimer channel leads to the formation of molecules on the repulsive side of scattering, as seen in the theory of FR [5].

Solving eq. (2.4.1) is done with the variational method by employing the Truncated Basis Method (TBM), first derived in [13]. The TBM approach consist of the regular minimization of the energy, i.e. $\partial_\lambda \langle H \rangle$, with respect to the expansion coefficients, λ_s , with the trial wave function:

$$|\Psi\rangle = \left(\lambda_0 c^\dagger + \sum_{\mathbf{k}} \lambda_{\mathbf{k}} c^\dagger \alpha_{\mathbf{k}}^\dagger + \frac{1}{2} \sum_{\mathbf{k}, \mathbf{p}} \lambda_{\mathbf{k}, \mathbf{p}} c_{-\mathbf{k}-\mathbf{p}}^\dagger \alpha_{\mathbf{k}}^\dagger \alpha_{\mathbf{p}}^\dagger + \lambda_0^{(M)} d_0^\dagger + \sum_{\mathbf{k}} \lambda_{\mathbf{k}}^{(M)} d_{-\mathbf{k}}^\dagger \alpha_{\mathbf{k}}^\dagger \right) |\psi\rangle, \quad (2.4.2)$$

where $|\psi\rangle$ is the wave function of a weakly interacting BEC, corresponding to the mean-field solution. By restricting the solutions to the form of eq. (2.4.2) the diagonalization of the Hamiltonian is reduced to eigenstates of this wave function, which significantly reduce the span of the Hilbert space. This wave function contains the BEC, the impurity and up to two Bogoliubov modes, along with a molecular channel and the three-body correlations.

Properties

The features of the polaron arising around the FR from these theories has been sketched in figure 2.2. On the bottom cartoon the impurity interaction with the medium has been indicated by the shading of the background, representing the BEC

medium. For stronger attraction between the impurity and the medium collects around the impurity creating and a local perturbation, represented by the polaron quasiparticle. And as the opposite happens for repulsive interaction a polaron is formed here. The formation of molecules between an impurity and a BEC atom through the molecular channel on the repulsive side, also known from the theory of FRs, is indicated by two orbs bound together. On the energy spectrum the perturbation from the medium on the bare transition leads to the formation of the two polaron states. The attractive polaron state E_a appearing from the side of the FR with negative scattering lengths, which diverge into lower energies as it approaches strong interaction at unitarity. For positive scattering lengths the repulsive polaron state E_r is formed rising towards higher energies as it approaches unitarity. Along with these the molecular state E_m is shown on the repulsive side. The Bogoliubov modes result in a tail of energy levels towards higher energies and the three-body correlations result in a broadening amongst all the energy levels. The many-body continuum resulting from these two effects has been depicted by the grayscaling.

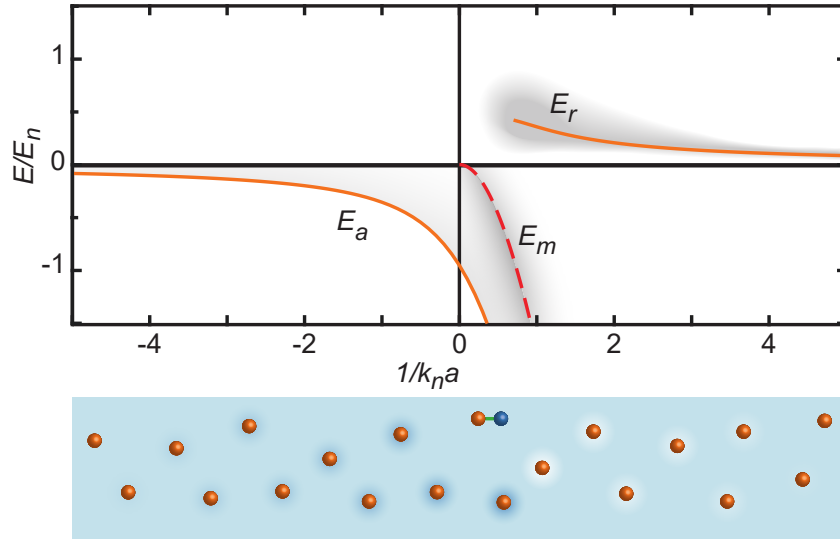


Figure 2.2: Sketch of the three major energy states arising around the unperturbed state (represented by the vertical zero line). Two polaron states (orange solid line); one from the attractive region E_a and one from the repulsive region E_r , is shown along with the molecular state E_m (red dashed line) The gray shading denotes the smearing of the states due to the many-body continuum. The bottom cartoon shows an impurity (orange orbs) in a medium (light blue shading), where the shading intensity represents the density of the medium around the impurity. Additionally the bond (green line) between a impurity atom and a medium atom (blue orb) indicates the possibility of molecular formation in the repulsive region.

Experimental Apparatus

The work of this thesis was carried out in the Mixtures laboratory in the Ultracold Quantum Gases Group, which had already achieved the preparation of a dual species condensate [6]. The apparatus for this thesis is the same as already build for the dual species condensation and only the experimental sequence differs. It is therefore the aim of this chapter to make a generic presentation of the experimental equipment and to highlight the features that will become relevant for the polaron experiment. Additional information can be found in [10, 14–16].

The chapter is structured as the following. First a brief overview of the experimental layout in section 3.1. Subsequently the laser systems necessary for trapping, cooling and imaging the atoms are presented in section 3.2. The Magneto-Optical trap (MOT) for loading the atoms is presented in section 3.3. Then a overview of the different magnetic traps and field control are given in section 3.4. Next the dipole trap, allowing for the trapping non-magnetically trapped states, is described in section 3.5. Then the state preparation of the system is described in section 3.6. The absorption imaging technique and optics are explained in section 3.7. Lastly, the creation of a dual species BEC is described in section 3.8.

3.1 Experimental overview

The experiment is build on two tables. One accommodates the vacuum system, the Magneto-Optical trap (MOT), the imaging system, along with the laser seed and amplifier for the optical dipole trap (ODT). On a second table the lasers systems, preparing the light for the MOT and imaging system, is mounted. By doing so the two systems vibrations are decoupled, which suppresses the failures of highly sensitive systems such as the laser locks. The laser light is tranferred to the science table by optical fibers.

The experimental sequence is run in two major stages. First the loading of atoms in the MOT cell, see figure 3.1, which are transported to the experimental cell, aka. science chamber. Both cells are made from glass to give optimal three dimensional optical access. The transport in between the two cells are done across a differential pumping stage, which provide about an order of magnitude of difference

in pressure of the vacuum, such that a relative high background of atoms is available for loading in the MOT cell, while still ensuring pressure below $1 \cdot 10^{-11}$ mbar in the science chamber, allowing for long lifetimes of the atomic samples in science chamber. The transport in between the cells is done mechanically by translating the quadrupole (QP) trap holding the atoms on a conveyor belt.

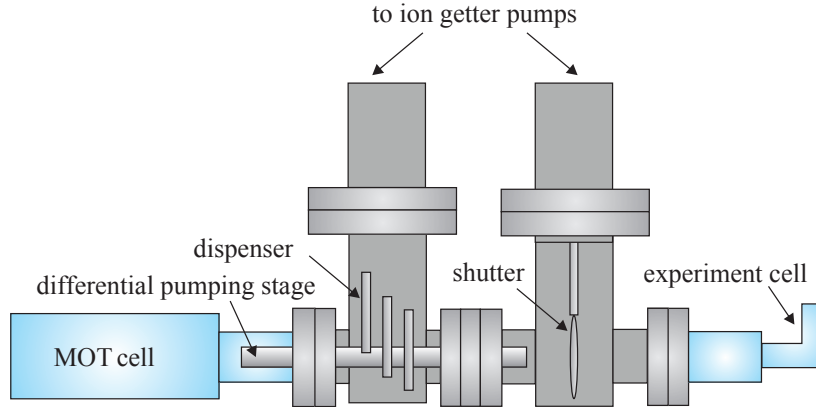


Figure 3.1: Vacuum system. Reproduced from [14]

The atoms for the MOT loading is provided by two non isotopes enriched dispenser sources, along with the light-induced atom desorption [17], which releases the atoms that have gotten stuck to the glass cell.

3.2 Laser systems

An overview of the necessary optical transitions is shown in figure 3.2 for both ^{87}Rb and ^{39}K . The repump light is used to pump atoms falling down into the $F = 1$ state back into the cooling scheme. The cooling light are used for magneto-optically trapping of the atoms in the MOT and for sub-Doppler cooling by slightly red detuning the light. Due to the small hyperfine splitting in potassium the repumper additionally has to be red detuned. The detection light is used for absorption imaging of the atoms in the end of the experimental sequence.

To realize the transitions in figure 3.2 the light is prepared on the laser table and brought to the science table by seven fibers. The MOT, dark spot (DS), repump and depump fibers are used in the DS MOT. Detection I, Detection II, and pumping fibers are used at the science chamber for imaging. The MOT, repump, optical pumping and detection fibers are shared between rubidium and potassium by combining both wavelengths with dichroic mirrors and coupling the combined beam into the same fibers. Shutters are individually placed before the couplers such that specific combinations of light can be configured individually in the experimental sequence.

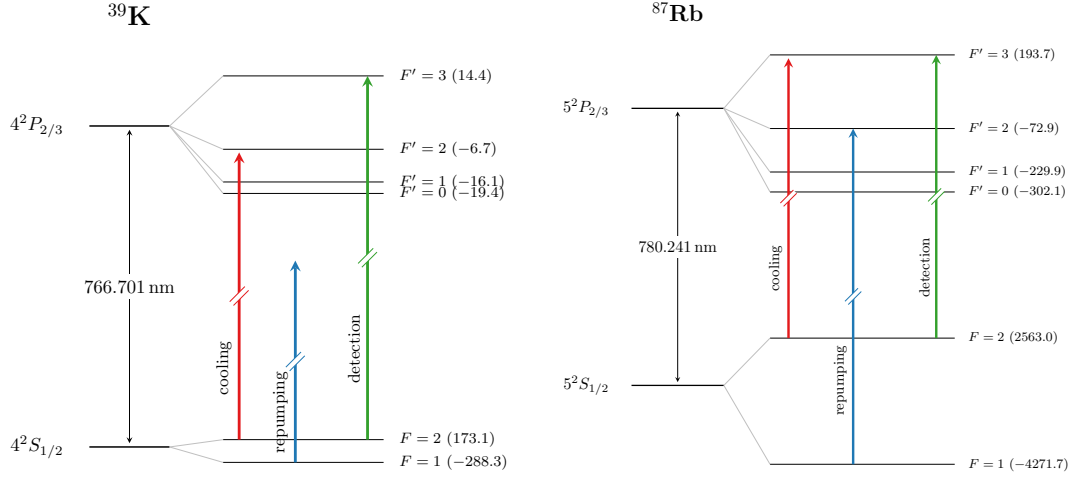


Figure 3.2: Relevant energy levels and hyperfine splittings, see parenthesis for splitting magnitude in MHz, for ^{39}K and ^{87}Rb . The cooling light (red arrow), the repumping light (blue arrow) and detection light (green arrow) is shown with detuning to scale to the upper hyperfine splitting. Note scales are different for each atom scheme. Adopted from [16].

3.2.1 Rb laser system

An outline of the rubidium laser system is shown on figure 3.3, while below the master and repump laser is described in detail.

The master laser is locked to the crossover resonance between the $|F=2\rangle \rightarrow |F'=2\rangle$ and $|F=2\rangle \rightarrow |F'=3\rangle$ in ^{87}Rb by utilizing saturated absorption spectroscopy (blue line) [18]. The spectroscopy light is shifted by 300 MHz by a double pass through an acousto-optic modulator (AOM), which frequency is used to modulate the frequency of the light to be able to derive an error signal for the spectroscopy. The light for the spectroscopy is provided by initially splitting the master laser up in this small part and a non-modulated part used in the following.

Part of the master laser light is then split up (purple line) and overlapped with the repump laser (green line) from RADIANTDYES) on a fast photo diode creating a beat signal that is recorded. From this the signal is used to stabilize the repump laser, via a so-called trombone lock. Note that a Fabry-Pérot cavity also overlaps the same two beams (red line for the master), this is occasionally used for examining the mode spectrum of the other lasers. These can be coupled into the cavity by optics not shown on the sketch. Another part of the master light (orange line) is split up to the pumping and depump fiber. This is matched to the $|F=2\rangle \rightarrow |F'=2\rangle$ transition by detuning the light 2×83 MHz through an AOM double pass. The rest of the light (red line) is shifted 410 MHz by an AOM double pass to match either the cooling or imaging transition, depending on the stage of

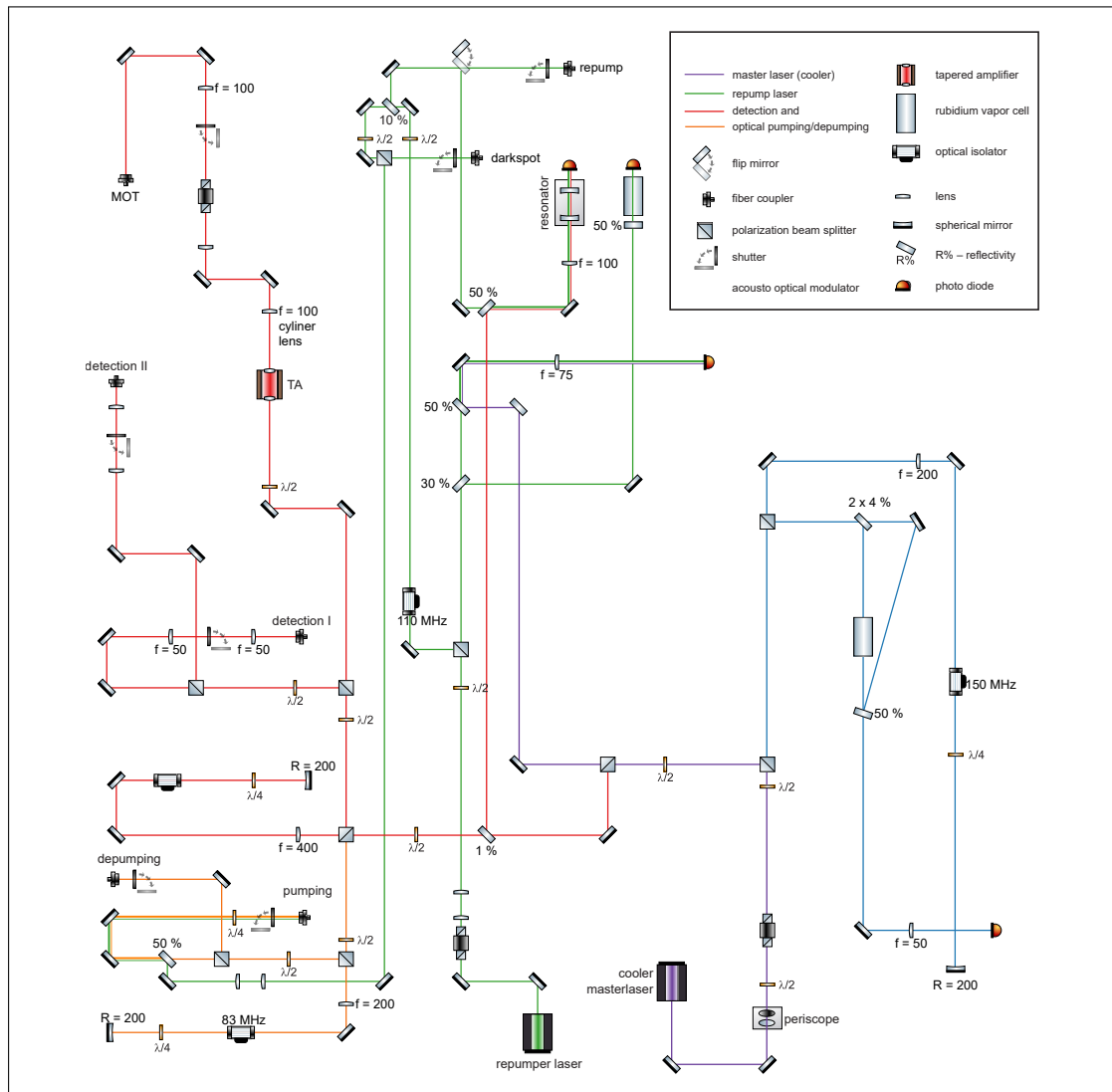


Figure 3.3: Rubidium laser system. Adopted from [14].

the experimental sequence. The light for the MOT is passed through a tapered amplifier (TA) which amplifies the light to about 800 mW.

The repump laser is shifted by a single pass AOM by 110 MHz then split up between the repump, DS repump and optical pumping fibers.

During the time of the thesis it was discovered that the repump laser diode and the TA medium had degraded over time, so both were replaced to reach reasonable powers and spectral parity.

3.2.2 K laser system

An overview of the potassium laser system is given in figure 3.4. A detailed description of the reference, cooling and repumping laser is given below.

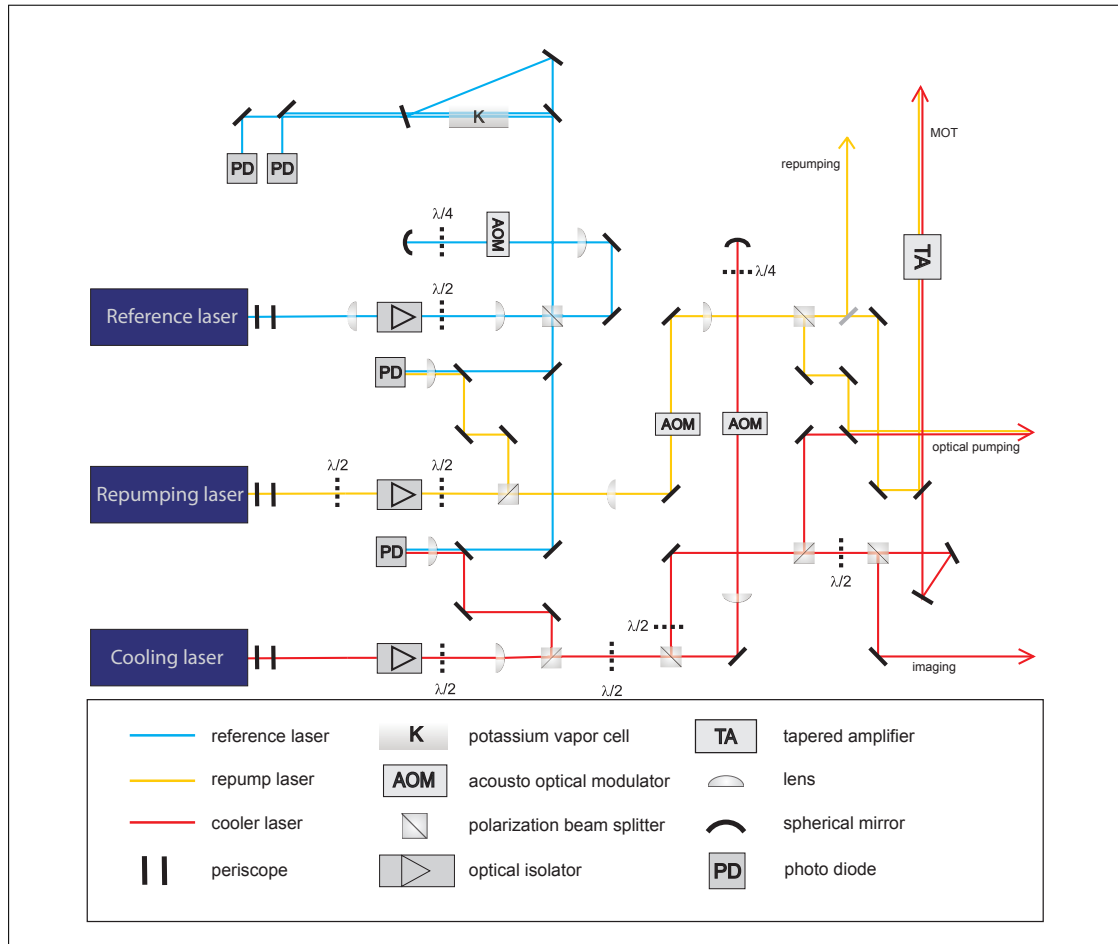


Figure 3.4: Potassium laser system. Adapted from [14].

The reference laser (blue line) is shifted by a double pass AOM to allow for a frequency shift of about 320 MHz. It is then locked to a ^{39}K crossover transition between the $|F=1\rangle \rightarrow |F'\rangle$ and $|F=2\rangle \rightarrow |F'\rangle$. Note that all the F' states are so close that they are regarded as one transition. This laser is split up into two references to make beat signals with the repumping (yellow line) and cooling lasers (red line). These are recorded by two fast photo diodes and compared to a reference, such that the beat frequency can be extracted for relative fixing with a phase-locked loop.

The repumping laser is sent through a single pass AOM, which allows for preparations of light for MOT, repumping or optical pumping, used at different stages of the experimental sequence.

The cooling light is frequency shifted by a double pass AOM to similarly prepare different frequencies for imaging, MOT and optical pumping at the different stages of the experimental cycle. They are then combined with rubidium light and coupled into their respective fibers.

The MOT and repump beams are overlapped and collectively sent through a TA gaining about 1 W of power. The rest of the beams are coupled into their respective fibers.

3.2.3 Laser characterization

During my thesis new laser systems were tested for potassium to acquire better linewidths at 767 nm than the existing home built laser systems [16]. For this I performed a complete test and wrote the following report characterizing two RADIANTDYES NARROWDIODE lasers.

The NarrowDiode lasers are interference-filter-stabilized external-cavity diode lasers and essentially follows the design published in [19]. In this design, the wavelength separation is realized by a low loss interference filter instead of the more common diffraction grating. This design yields high robustness against mechanical and thermal disturbances and provides a spatially fixed output beam. Thus, the direction and position of the output beam are largely independent of the output wavelength. The two lasers under investigation were intended for cooling and trapping of the isotopes of potassium. Thus, all optical elements were chosen for a wavelength of approximately 767 nm, matching the D_2 line [20].

Since these lasers previously preformed unreliably, the tests described here were preceded by a fault diagnosis and subsequent changes to the lasers by RADIANT DYES. Based on our research group's experience with potassium laser systems of similar design, our hypothesis was that the anti-reflection coating of the (previously used) laser diodes with a center wavelength of 790nm were damaged. This can lead to

the counter intuitive behavior that the laser diodes yield more power, thus seemingly performing better. At the same time, however, the tuning range is strongly reduced due to the damaged coating and the lasers can not be operated at the wavelength of 767 nm anymore.

A comparison with other available laser systems at 767nm showed, however, that the latest generation of diode lasers designed for a wavelength of 780nm may indeed be a better candidate for a laser operating at 767nm and we therefore recommended such a laser diode. Based on this recommendation, RADIANT DYES used the laser EYP-RWE-0780-02000-1300-SOT12-0000 by Eagleyard Photonics in the tested laser systems.

To assess the suitability of these lasers for cooling and trapping of potassium, we have performed the following tests. The output power was measured as a function of current, saturated absorption spectroscopy on a thermal potassium gas was performed with both lasers, and the spectral characteristics were investigated by measuring the beat signal between the two lasers.

The two lasers under investigation have the serial numbers 1614 and 1616. They were operated with controllers supplied by RADIANT DYES with the serial numbers 1562 (04/13) and 1616 (10/13), respectively. In the following they will be referred to as 1614 and 1616.

Installation of the lasers were done on an optical table to perform the measurements detailed in the following. After connecting to their respective controllers, both lasers emitted light as expected. Initial measurements with a wavemeter and subsequent spectroscopic measurements showed that the unit 1616 was lasing at a wavelength close to the potassium transition wavelength. The other unit however, had drifted further from the design wavelength and a small adjustment of the interference filter was required to reach the potassium transition wavelength. No further adjustment of the filter has been required since.

Laser diode threshold characterized by the power output of the two diode lasers is shown in Fig. 3.5. The lasing threshold of 55 mA and 52.4 mA for the lasers 1614 and 1616, respectively is slightly different, most likely due to the cavity alignment. The current was obtained from the built-in current display of the controller and the monitor output. The output power was measured with a calibrated power meter. The output was not increased beyond 20mW, since the exact laser diode specification was unknown to us at that time.

The output power to current ratio is 0.8245 mW/mA for the laser 1614 and 0.6659 mW/mA for the laser 1616. This difference results in similar output power of approximately 20mW at 80mA.

Doppler-free spectroscopy were performed to access the possibility for stabilization to an atomic transition, which is necessary for the laser capabilities for

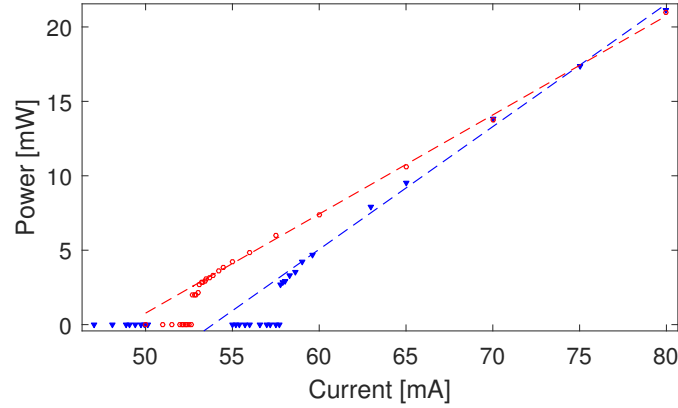


Figure 3.5: Output power as function of current for the 1614 (blue triangles) and 1616 (red circles) lasers.

cooling and trapping of neutral atoms. In the case of potassium, the lasers are typically stabilized to the Doppler-free spectroscopy signal of ^{39}K which is the most abundant isotope (93%). Such a spectroscopic measurement also provides a first indicator of a laser's spectral characteristics, since the transitions typically can not be resolved properly if the laser does not run single mode.

Doppler-free saturation spectroscopy was performed on the ^{39}K D2-line in a heated glass cell ($\approx 45^\circ$) with both lasers. The lasers were tuned to this frequency using the temperature, the current and the retroreflecting cavity mirror. The spectra were recorded on a large area photo diode (Thorlabs PDA36A-EC) while the laser was scanning at a rate of 500Hz.

The spectra of the two lasers are shown in Fig. 3.6. The Doppler broadened spectrum was subtracted from the signal, such that only the features of the ^{39}K D2-line are present. Due to the small hyperfine splitting of potassium this spectrum can not be assigned to individual transitions. Essentially, the large positive peak can be attributed to all $F = 2 \rightarrow F'$ transitions, while the large negative dip is the ground state crossover feature. The frequency axis in Fig. 3.6 was obtained by assuming a 224 MHz frequency difference between these features [21] and a linear frequency sweep. The small additional feature in both figures is attributed to all $F = 1 \rightarrow F'$ transitions. This spectrum is equivalent to the one obtained with all previous laser systems in our laboratory and corresponds to the one published in [22].

In Fig. 3.6, the signal size and signal-to-noise ratio is better for the laser 1614, however this is due to our optical setup rather than the laser itself, since this laser optical path provided lower power. Based on this spectroscopy the lasers perform equally well and match the performance of TOPTICA DLPRO lasers tested in our laboratory.

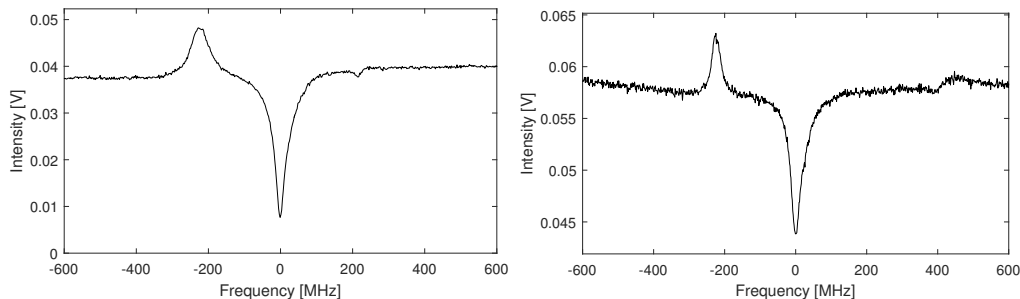


Figure 3.6: Doppler-free saturation spectroscopy signal of the lasers 1614 (left) and 1616 (right).

Beat spectra were recorded to determine the linewidth of the lasers. For this purpose light from both lasers was superimposed on a beam splitter and coupled into a single-mode optical fiber. This yields good mode overlap and thus ensures a high signal-to-noise ratio. Both lasers were running freely in close vicinity to the K transition frequency and the relative frequency was set using the retroreflecting cavity mirror. The beat signal was recorded on a fast photo diode (Thorlabs DET10A) positioned after the optical fiber.

Multiple beat signals were recorded on a spectrum analyzer. Figure 3.7 shows a typical beat spectrum from this data set recorded at a frequency offset of approximately 54 MHz. The spectrum analyzer was set to a sweep duration of 5 ms, a resolution bandwidth of 200 kHz and video bandwidth of 50 kHz. The beat signal corresponds to the sum of a Lorentzian due to the high frequency noise of the laser and a Gaussian due to the drift of the the laser within an individual measurement. The beat signals were therefore fitted with Gaussian in the central region ($|\Delta\nu| < 0.5$ MHz) and a Lorentzian in the wings ($|\Delta\nu| > 1$ MHz) as in the original characterization [19]. An average over 10 data sets yields a Gaussian FWHM of 208(12) kHz and a Lorentzian FWHM of 24(8) kHz.

This result is essentially equivalent to the one previously published for different wavelengths [19]. The slightly larger Gaussian FWHM measured here is likely due to the fact that both lasers were running freely during the measurement and thus an additional drift could occur during the chosen sweep time.

This spectrum shows that the NarrowDiode laser system in its tested configuration is very well suited for laser cooling purposes. Due to the small inherent linewidth of the laser indicated by the Lorentzian FWHM, it should be possible to stabilize the laser with high precision to an appropriate reference.

Summarizing the laser systems were found to perform to the specifications provided by RADIANT DYES equivalent to those given in [19]. The spectrum obtained from Doppler-free saturation spectroscopy was equivalent to that typically observed in our laboratory and published results [22]. The beat spectrum shows that

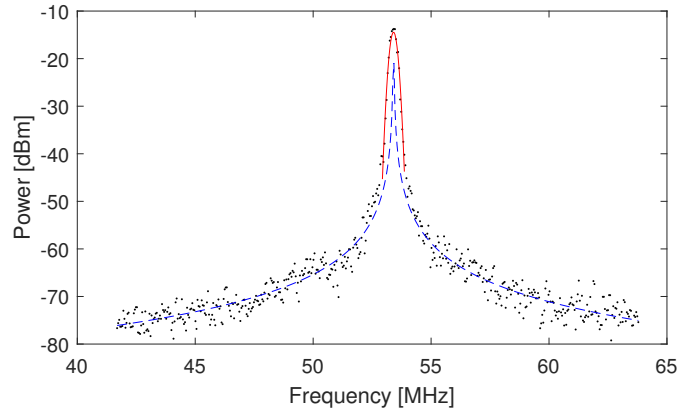


Figure 3.7: Beat signal recorded at a frequency difference of approximately 54 MHz with spectrum analyzer settings of sweep duration 5 ms, resolution bandwidth 200 kHz and video bandwidth 50 kHz. The Gaussian and Lorentzian fits are indicated.

the lasers have a particularly narrow linewidth, which allows for precision stabilization. This feature surpasses other available laser systems in our laboratory. Apart from an electrical failure of the controller, the system has proven to be stable in day-to-day operation.

The tests were conducted at an output power of approximately 10 mW. A test of the tuning range of the laser was not conducted.

In conclusion, the laser is highly suitable for applications in laser cooling and trapping. Due to its narrow inherent linewidth it surpasses the requirements on linewidth for laser cooling of K considerably.

3.3 Magneto-Optical Trap

The atoms are initially collected and prepared by trapping them in the MOT, which consists of a magnetic field provided by two coils in an anti-Helmholtz configuration, and six counter-propagating light beams. The polarization of the beams is cleverly chosen such that they selectively match the energetically lower-lying hyperfine state, which is shifted outwards from the trap center due to the Zeeman effect, see figure 3.8. Additionally, the detuning of this trapping light leads to Doppler cooling of the atoms.

Loading two atomic species leads to additional requirements for the MOT. Light-assisted collisions, where one or both atoms are excited into an attractive molecular potential, can lead to channels of loss and heating. Either the de-excitation of the state can go into a bound molecular state that is not confined by the trap or the light emitted, when falling into a lower-lying energy level, can be more red-detuned than the collective light initially exciting the atoms, leading to a total gain in kinetic energy. To reduce these effects, the rubidium MOT is

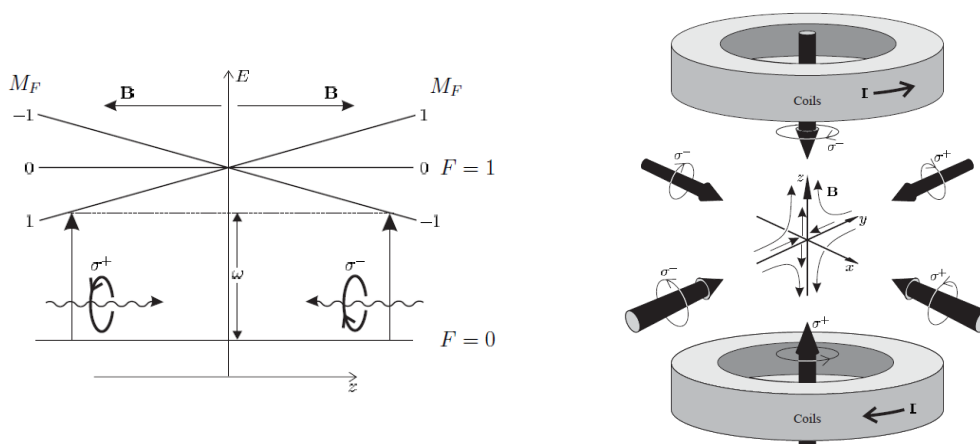


Figure 3.8: General construction of three dimensional MOT. (a) A simple illustration of how the QP field spatially rises outwards from the center of the trap, leading to a spatially dependence Zeeman splitting. The axis of rotation is opposite to the magnetic field direction. (b) Outline of the three dimensional MOT configuration. Adopted from [15].

modified into a dark spontaneous force magneto-optical trap, or dark-SPOT MOT. The concept is simply to remove the rubidium repump light in the center of the trap. For this the rubidium system has separate repumper and cooling light, while potassium can still be supplied jointly. This is done by widening the beam through a telescope and placing a opaque disk with a dark spot with diameter 6 mm in the beam path, see figure 3.9, blocking the light in the center of the beam. Atoms at the center that can fall into the non-trapped $F=1$ state will then drift slowly out of the screened area and be re-excited into the closed optical cycling. They are spatially confined by reusing the light forming a bicylinder Steinmetz confinement. Additionally the rubidium depump beam driving the $|F'=2\rangle \rightarrow |F=2\rangle$ transition is added at the center, pumping as many atoms from the undesired exited state.

To estimate the number of atoms collected in the MOT, the florescence is recorded on a photo diode. For recording of a specific species the light can be tuned onto resonance of one, while tuning of the light for the other.

In figure 3.10a the effect of the MOT configurations is shown. It is clear that the presence of a conventional rubidium MOT sets an upper limit for the loading of the potassium atoms. With the DS MOT simultaneous loading of rubidium is possible while keeping the number of potassium atoms almost at the same level as without a rubidium MOT. Most of the gain is achieved during the first 25 s and in practice the loading time is optimized with respect to the number of atoms and temperature in the end of the sequence.

After fixing the loading time to 25 s the spatial trade off between rubidium and potassium due to the dark spot diameter is investigated, see figure 3.10b. The

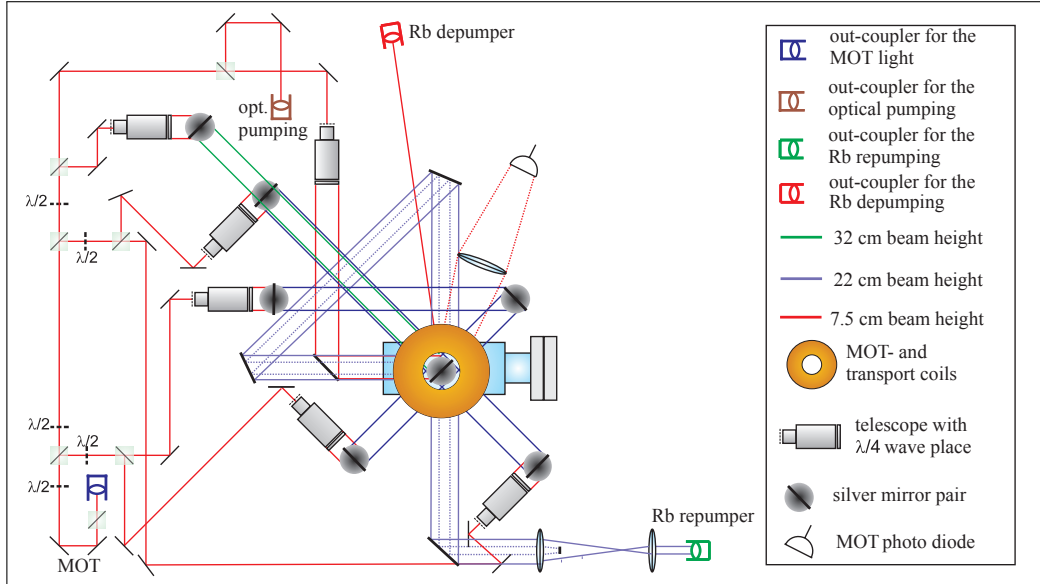


Figure 3.9: Sketch of DS MOT. Adapted from [14].

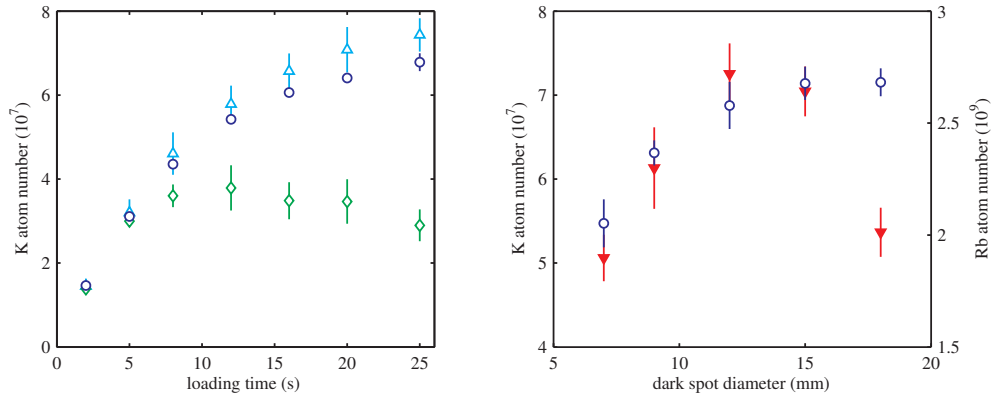


Figure 3.10: MOT loading dependence on the MOT configuration and diameter of dark spot. (a) ^{39}K atom number as a function of time in the presence of a ^{87}Rb DS MOT (dark blue circles), a conventional ^{87}Rb MOT (green diamonds) and in the absence of any type of ^{87}Rb MOT (cyan triangles). (b) Number of ^{39}K (dark blue circles) and ^{87}Rb (red triangles) as a function of DS diameter. Adapted from [10].

change simply done by translating the dark spot closer or further away from the telescope. It is clear an optimum can be found between 12 mm to 15 mm. 12 mm was chosen since the loss of rubidium atoms compared to gain in potassium atoms disfavored.

After the MOT loading the two species are cooled to the Doppler limit by turning off the magnetic field and detuning the cooling light. For rubidium the cooling light is detuned to -7 times the natural linewidth Γ from resonance during a duration of 9 ms. For potassium the repump light is turned down to 5 % of its initial power and tuned to resonance. This leads to low population of the bright states and thereby regulates the photon scattering of the cooling light. The cooling light is then detuned to -0.5Γ and ramped to -2.3Γ while simultaneously lowering the power linearly to 50 %.

The two species are finally prepared for magnetic transport by optically pumping them to the low field seeking $F'=2$ state. This is done by applying σ^+ polarized light resonant with the $|F=2\rangle \rightarrow |F'=2\rangle$ transition for 1 ms. The repump light is additionally applied to repump decayed atoms.

3.4 Magnetic Trap and field control

Besides sets of field compensating coils, there are only two main sets of coils present in the experiment, the coils mounted on the conveyor belt and the coils in the science chamber, see figure 3.11. However, these are involved in many different configurations during the experimental sequence.

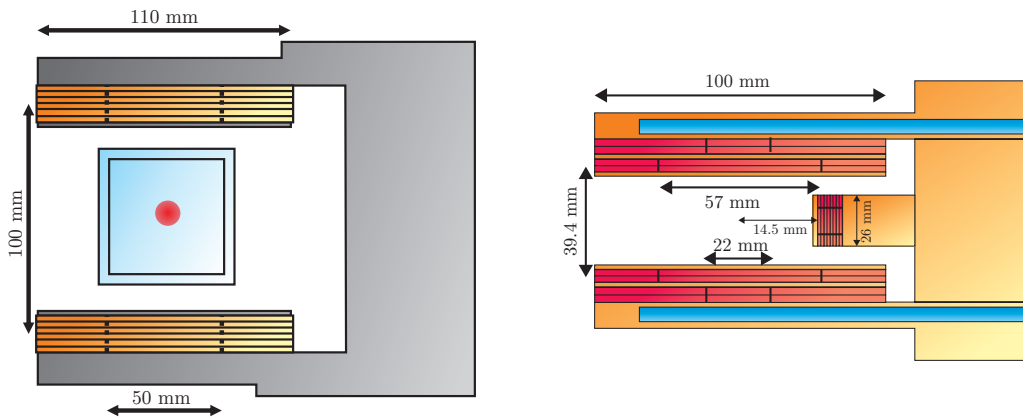


Figure 3.11: Coil sets. The profile of the transport/MOT coils (a) which are mounted on a conveyor belt. The stationary science coils (b) including two sets of Helmholtz coils and the Ioffe-coil. The blue area shows the water cooling channels. Adopted from [14].

3.4.1 MOT and Transport coils

The aforementioned transport coils initially pose as the QP trap of the MOT. Here the coils are run in the anti-Helmholtz configuration at 2.5 A to provide a field gradient of 11 G cm^{-1} .

The same configuration is used during transport but here the current is abruptly put to 15 A to catch the atoms. Over 50 ms the current is then ramped to 45 A providing a field gradient of 196 G cm^{-1} to strongly confine the atoms during transport. The magnetic coils are then translated on the conveyor belt to the L-shaped science chamber, see section 3.1.

3.4.2 Magnetic Trap

In the science chamber the atoms are then loaded from the transport coils to the science chamber coils by lowering the field of the transport coils over 800 ms and ramping up the science coils to a QP field gradient providing 350 G cm^{-1} . The field is stabilized by water cooling the coils to $19.0(1)^\circ\text{C}$.

The QP field is provided by the four Helmholtz coils in the science chamber by configuring them in a anti-Helmholtz configuration. This is one of the configurations that these coils can be arranged in by specific direction of the current through the coils with the four MOSFETs seen figure 3.12. The possible configurations are as follows:

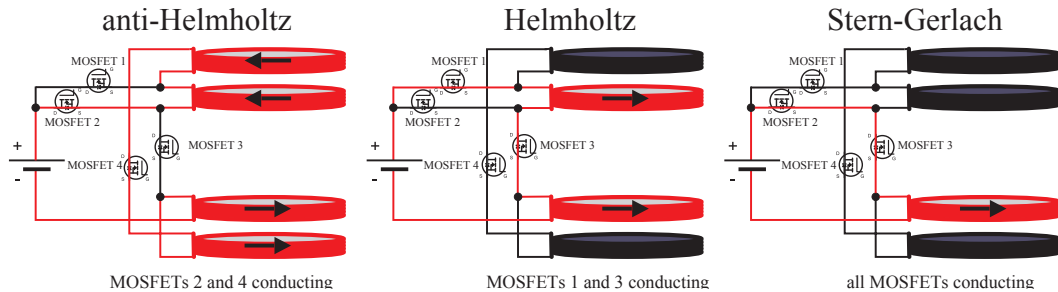


Figure 3.12: Science chamber coils and MOSFETs diagram. Adapted from [14].

Anti-Helmholtz configuration provides the QP field for initial trapping of the atoms in the science chamber. This configuration is also used in addition with the Ioffe-coil, the small coil in see figure 3.11b, to create the Ioffe-Pritchard configuration (QUIC).

QUIC is used in sympathetic cooling where the Ioffe-coil field raises the trap bottom. Here the current applied through the Ioffe-coil creates a magnetic field towards itself, providing an offset field in the center of the QP trap. As the current is increased and the trap center moves towards the coil a harmonic potential will be

formed with a non-zero field center. This is done to avoid Majorana spin flips that happens at the QP trap center where atoms has no preferred spin direction in this region, since the field is zero. Additionally unwanted spin states can be removed since their individual splitting in the trap center diffees, this will be described in the following.

Helmholtz configuration can apply a homogeneous magnetic field over the atoms used for the Zeeman splitting in state preparations and in experiments involving magnetic field dependence. Additionally this provides the field with which the scattering length is tuned via the magnetic FR.

Stern-Gerlach configuration, applying a field gradient in time of flight (ToF) can spatially separate the atoms of different spin states. This is used to imaging for detecting the state configuration.

3.4.3 Evaporative cooling

^{39}K is not well suited for cooling to BEC by itself so the way to reach high enough phase-space density (PSD) is by mostly do evaporative cooling on ^{87}Rb and let it rethermalize with the ^{39}K . This procedure is called sympathetic cooling and is done in three steps to reach dual species condensates, see figure 3.19.

The first part of the sympathetic cooling is done in the QP trap as it provides high thermalization rates. The QP field provides a position dependent splitting of the internal spin states, see figure 3.13. The evaporative cooling is here done with microwave (MW) transition on the $|2,2\rangle \rightarrow |1,1\rangle$ transition rather than with radio frequency (RF), since the difference in hyperfine splitting allows for addressing of only rubidium and not potassium. The hottest atoms will subsist on the edge of the QP trap, where they are evaporated away by the MW knife ramped from $\nu_0 + 135$ MHz down to $\nu_0 + 30$ MHz over 5 s. Here ν_0 is the unperturbed $|2,0\rangle \rightarrow |1,0\rangle$ transition. This cooling in the QP trap cannot be extended all the way to quantum degeneracy since Majorana spin flips in the center of the trap, leads to losses. As the $|1,1\rangle$ atoms are leaving the trap the energy difference between the $|1,1\rangle$ and $|2,1\rangle$ state may become resonant with the MW knife, where a occupation of atoms might build up. This is problematic since the atoms gain kinetic energy in between the two transitions, i.e. heating occurs. However both of these issues can be addressed by raising the trap bottom as in the QUIC trap and additionally applying a second MW source driving the $|2,1\rangle \rightarrow |1,1\rangle$ at zero field, removing the unwanted atoms. The MW knife can then be continued down to $\nu_0 + 2.54$ MHz over 28 s.

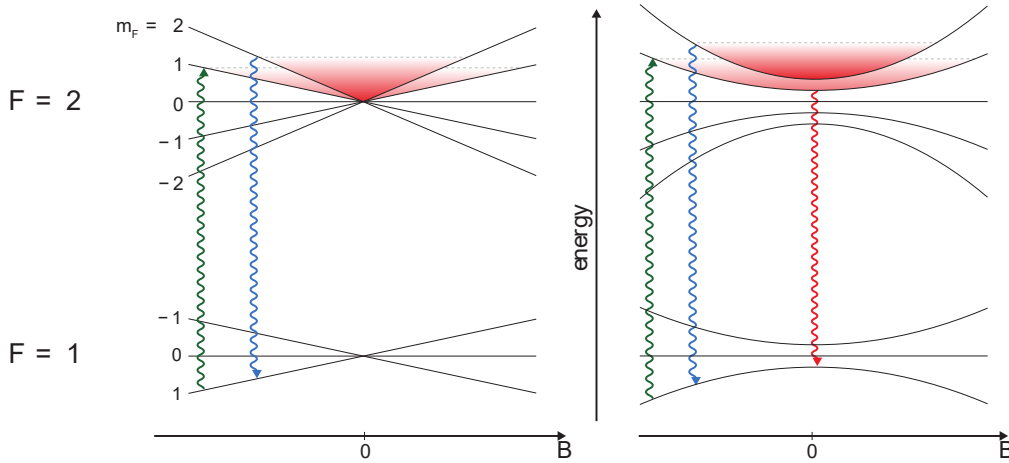


Figure 3.13: Spin state potential dependence on the magnetic field position for (left) the QP trap and (right) the QUIC trap. The evaporative MW knife (blue wiggly line) transfers the hot atoms on the edge of the trap to the untrapped $|2,2\rangle \rightarrow |1,1\rangle$ state. As the $|1,1\rangle$ atoms leave the trap the shift of the $|1,1\rangle \rightarrow |2,1\rangle$ can become resonant with the very same MW knife (green wiggly line). For the QUIC trap these re-introduced $|2,1\rangle$ atoms are avoided by transferring them to the untrapped state by an additional MW transition (red wiggly line). Adapted from [14].

3.4.4 Magnetic field compensation

To compensate for the external magnetic field seven magnetic coil sets in a Helmholtz configuration are mounted on the science table. Three big coil sets, one for each dimension, are mounted along the edges of the science table on the meter scale. These provide a static field compensating for the external field offset to zero. This offset compensation is enough to run the MOT. Besides this a more precise compensation is achieved around the science chamber by three additional sets. These are mounted in the near vicinity of the chamber on the decimeter scale. This field as well is static. Lastly an additional active compensation is done in the vertical direction by an additional coil set around the table edge. These compensate for fluctuations, such as the 50 Hz noise, by applying a field with opposite phase. To do so the field is controlled with a proportional-integral-derivative (PID) loop. Besides this, for high precision magnetic fields, the science chamber coils can be switched to a battery source to avoid any influence from the 50 Hz noise leaking from the electric grid through the power supply.

3.5 Optical dipole trap

The optical dipole trap (ODT) relies on the force from the electric field of the light on the atoms due to the dipole moment, induced by the field itself. Two effects arise from the atom-light interaction for a Gaussian light beam detuned

much greater than a linewidth Γ from the transition resonance ω_0 . Namely the dipole trapping potential [23]

$$U_{dip}(\mathbf{r}) = \frac{3\pi c^2}{2\omega_0^3} \left(\frac{\Gamma}{\Delta} \right) I(\mathbf{r}), \quad (3.5.1)$$

, and the scattering rate

$$\Gamma_{sc} = \frac{3\pi c^2}{2\hbar\omega_0^3} \left(\frac{\Gamma}{\Delta} \right)^2 I(\mathbf{r}), \quad (3.5.2)$$

where c is the light speed and Δ is the detuning. For a red detuned Gaussian beam the atoms will feel a force towards the center of the beam, where the intensity is highest. The scattering of photons will apply a net force away from the source, pushing the atoms along the axis of the beam. But as is clear from equations (3.5.1) and (3.5.2) the scattering rate falls off with respect to detuning than the trapping potential. Therefore the light is far detuned, by using a 1064 nm light source, which is far from both the 767 nm and 780 nm, for potassium and rubidium respectively. By crossing two dipole beams the atoms can be strongly confined in alle dimensions.

The high intensity light is provided by a separate laser system on the science table, consisting of a monolithic ring laser (COHERENT MEPHISTO) amplified by a fiber amplifier, see figure 3.14 (NUFERN PSFA-1064-50MW-50W-0). Afterwards the light is divided into two and passed through AOMs, coupling the first order into the fibers going to the experiment, such that the beam powers can be controlled by distribution into the first order.

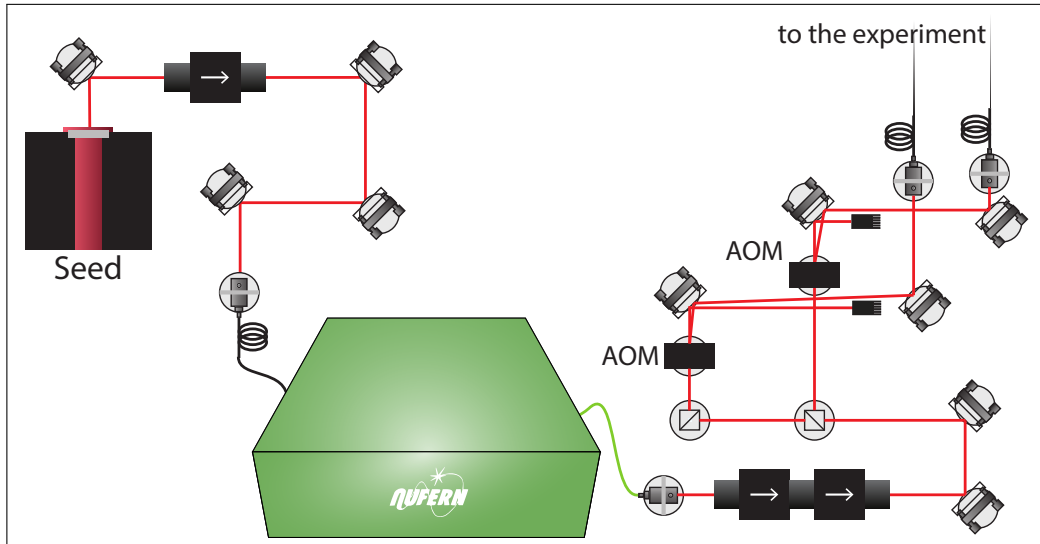


Figure 3.14: Dipole laser system and power regulation. Adapted from [15].

The two beams are then brought to the science chamber by fibers and by dichroic mirrors that are reflective to only the dipole beam and not the detection

light, see figure 3.15. The loading into the dipole trap is done by ramping down the current through the QUIC coils while ramping up the intensity of the dipole trap to 1500 mW. This provides a harmonic trap with frequencies of $\nu_x = 158$ Hz, $\nu_y = 167$ Hz and $\nu_z = 228$ Hz for a beam waist of $100 \mu\text{m}$.

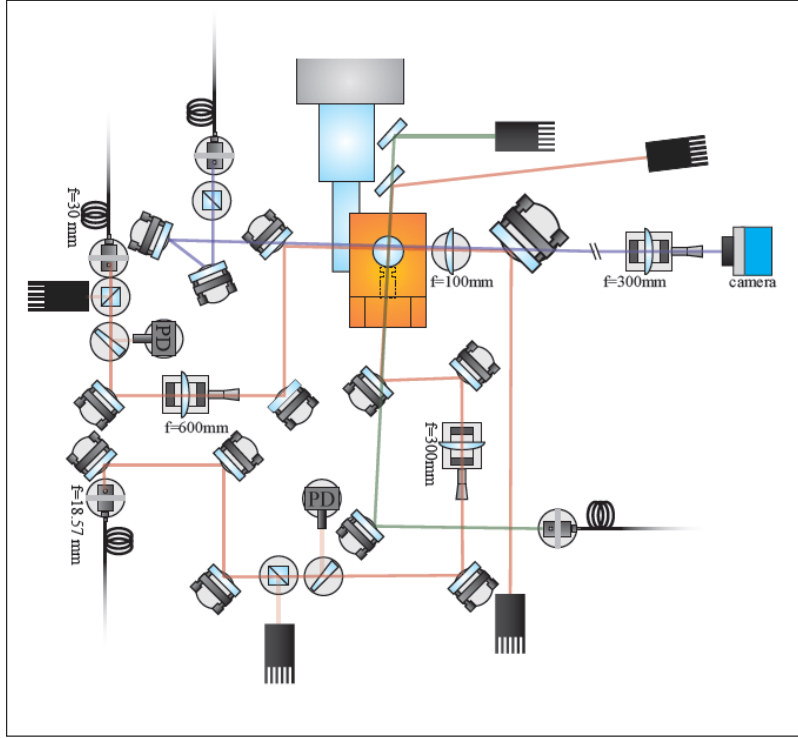


Figure 3.15: Science chamber optics. Adapted from [15].

The trap depth dependence on the dipole power for potassium and rubidium is shown on figure 3.16. From right to left the edges the curves show when the atoms goes from escaping the horizontal trapping to escaping vertical trapping due to the gravitational sag. Along with this the immersion of the potassium in rubidium is shown on the second axis. This is important since as much sympathetic cooling on potassium is desired when evaporating the rubidium. The waist of the beam was adapted to achieve this. In fact the black dotted vertical line indicates when a ^{39}K BEC of about $2 \cdot 10^5$ atoms is reached. If the power is decreased below 450 mW the rubidium is lost and a pure potassium sample is prepared.

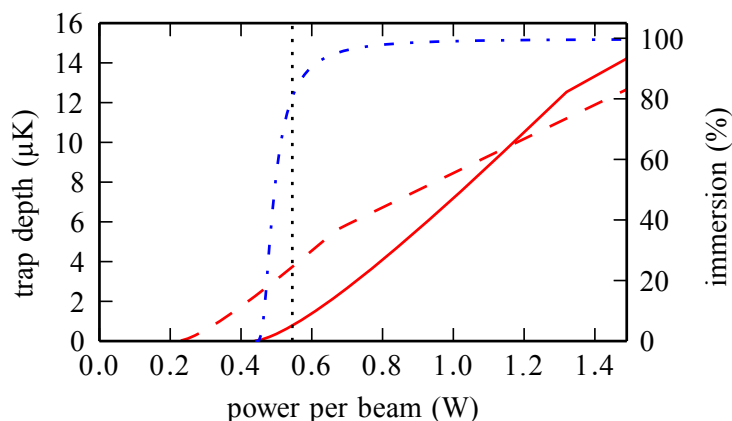


Figure 3.16: Optical trap depth against the applied dipole power for ^{39}K (red dashed line) and ^{87}Rb (red solid line). The immersion of ^{39}K in ^{87}Rb (blue dash dotted line) has a steep edge as the trap becomes weak for ^{87}Rb and the differential gravitational sag becomes important. The black dotted vertical line shows the expected power at which condensation of the BEC atoms occurs. Adapted from [10].

3.6 State preparation

Cooling potassium straight to BEC in a magnetic trap is problematic since it has a negative background scattering length, which will lead to a implosion of the cloud when condensed, the so-called Bose-nova. The atoms are therefore transferred into a dipole trap in the science chamber where an external magnetic field can be applied to employ a FR that provide a positive scattering length for potassium. Even further the spin state field dependence is no longer needed to trap the atoms and it is therefore possible to transfer the atoms to the $|1,-1\rangle$ state where there is a strong inter-species FR available proving strong rethermalization between potassium and rubidium, see figure 3.17.

To make the state preparation for the sympathetic evaporation in the dipole trap ($|2,2\rangle$ to $|1,-1\rangle$) the atoms are transferred in a three step process. First an adiabatic passage transfers both species to the $|2,-2\rangle$ state by sweeping RF radiation from 6.0 MHz to 8.2 MHz over 2 ms in a homogeneous background field of 10 G. Secondly the rubidium is transferred to the $|1,-1\rangle$ state by applying a resonance MW π -pulse at a background field of 1.8 G over 6 μs . Thirdly the potassium is transferred to the $|1,-1\rangle$ by sweeping the background field from 15 G to 3.5 G while irradiating the atoms with a RF field of 450 MHz.

The disadvantage of transferring potassium before rubidium would be that this opposite process will leave rubidium in a higher energetic hyperfine $|2,-2\rangle$ state compared to the potassium and therefore spin changing collisions will have excess energy that will lead to heating of the sample.

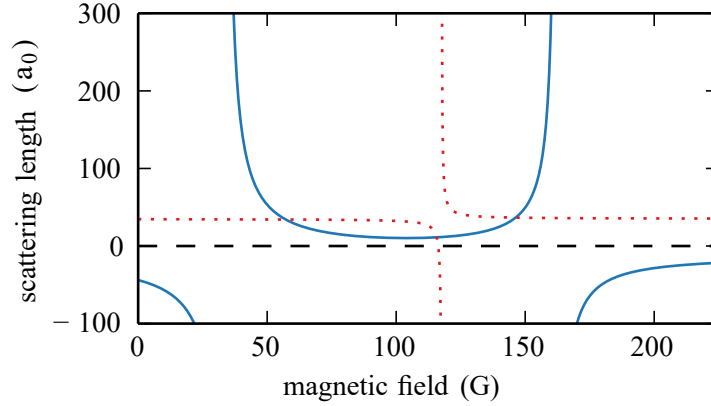


Figure 3.17: FR relevant for cooling with the $|1,-1\rangle$ state. Here the intra-species scattering length of ^{39}K (blue solid line) is positive between two FR at 33.6 G and 162.25 G. The inter-species scattering length can be tuned with a FR located about 117.56 G (red dotted line). Adopted from [10].

3.7 Absorption imaging

Finally, a measurement on the atoms are performed by applying absorption imaging on both species after free expansion. The final magnetic field of the experiment is kept at the same value for the first 6 ms of the expansion to avoid any non-linear effects on the interaction, such as crossing one of the FRs. Afterwards the clouds expand ballistically, so the magnetic field can be turned off. The decay of the field to a background value of 1 G last about 12 ms so to avoid any related effects the imaging is taken after 23 ms ToF. The imaging is performed on potassium first and 2 ms later on rubidium limited by the readout time of the camera. This allows to image both species in the same experimental sequence. The exposure time on the camera is 38 μs . The imaging beam is resonant with the $|F=2\rangle \rightarrow |F'=3\rangle$ transition so the atoms are repumped 200 μs before the imaging and the repump light kept on during the imaging. The state composition is imaged by applying a inhomogeneous magnetic field, applied with the Stern-Gerlach configuration, for 5 ms of the expansion. The camera chips is cleaned by taking a dummy image just before the real images, and the fan for the camera is turned off to avoid vibrations.

As the light propagates through the cloud its intensity is attenuated depending on the column atom density \tilde{n} as

$$I_{atoms}(x,y) = I_{beam}(x,y) \cdot e^{-\tilde{n}(x,y)\sigma},$$

where I_{beam} is the beam intensity and σ is the effective cross section, which has

the following relation to the cross section σ_0 at resonance

$$\sigma = \frac{\sigma_0}{1 + 2\frac{I}{I_{sat}} + \left(\frac{4\Delta^2}{\Gamma^2}\right)}, \quad (3.7.1)$$

where I_{sat} is the saturation intensity, Δ is the detuning from resonance and Γ is the resonance linewidth. The optical density can then be determined by logarithmically subtracting the intensity I_{atoms} from I_{beam} . An example is shown in figure 3.18. The average column density can, neglecting multiple scattering events, be determined by dividing the optical density with eq. (3.7.1). A formula that takes the scattering into account, by introducing the experimentally determined α factor, has been adopted in our experiments [24]. The average density for a pixel is then given by

$$n = \left(\alpha(\log I_{ref} - \log I_{atoms}) + \frac{I_{ref} - I_{atoms}}{I_{sat}} \right) \frac{1}{\sigma_0}.$$

The α -calibration is done by evaluating a data-set for different intensities and evaluating this with different α -values. As the atom number evaluation should not vary with intensity α is chosen as the value that has the lowest variance with respect to the different intensities. During the thesis the α factor was recalibrated for ^{39}K to 1.57 instead of 1.11. The evaluation of the optical density is done in the PERFECTFIT software developed in the group. And further evaluation can be applied in this software such as the bimodal fit of a thermal and BEC distribution.

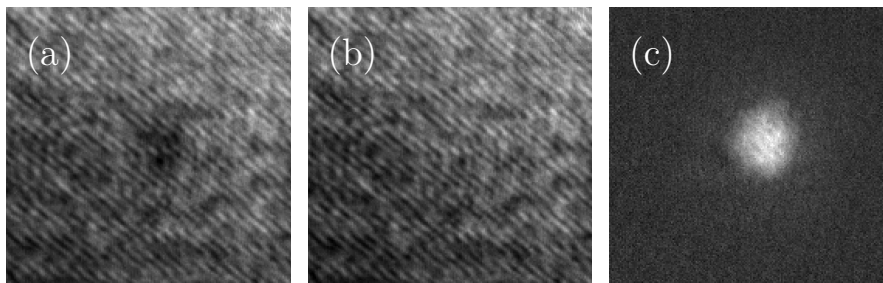


Figure 3.18: Absorption imaging sequence. The image taken with the cloud present (a) is subtracted from the reference beam image (b) without any atoms to get the optical density (c). The fringes present in the difference occur because of small vibrations that moves the camera in between the two pictures (a&b). Adopted from [15].

3.8 Dual species BEC

The loading of the atoms into the dipole trap and state preparation lead to a losses of both species, which can be observed as a jump in figure 3.19. When this has been accomplished, the final step of evaporation can be initialized. The

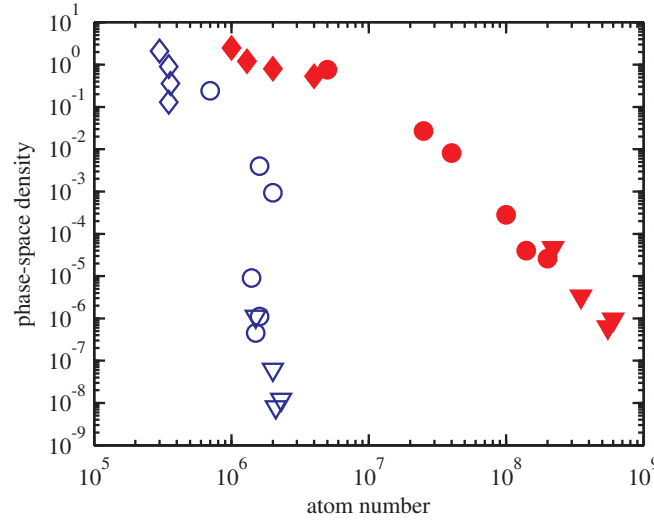


Figure 3.19: PSD against the number of atoms of ^{39}K (red) and ^{87}Rb (blue). The number of atoms for especially ^{87}Rb are traded off for higher PSD in evaporative cooling in the QP trap (triangles), the QUIC trap (circles) and the ODT (diamonds). Adapted from [6].

positive scattering length of the potassium, accessible in the region between the two intra-species FRs, see figure 3.17, is addressed by tuning the magnetic field in this region. The evaporation is chosen to be on the positive side of the inter-species FR. No significant gain in cooling is observed by staying close to the inter-species FR, so in practice the evaporation is done at 142.5 G since many experiments are accessible from this point. A homogeneous field is provided by the magnetic trap in the Helmholtz configuration. To achieve high precision magnetic fields the background field is actively stabilized in the vertical direction and the current is provided by the battery supply. When the magnetic field has reached 142.5 G the evaporation is performed by lowering the ODT power from 900 mW to 480 mW. Along this path a rubidium BEC is first formed followed by a potassium BEC as the two species rethermalize, see figure 3.19. The figure also illustrates how the evaporation mainly occur on rubidium in each step.

Additional steps utilizing apparatus mentioned above can now be applied in the sequence to perform dual species experiments.

Measuring the Bose polaron

As already established in previous sections a clever choice of a FR opens a variety of possibilities. When the polaron experiment was first considered it seemed straightforward to prepare the dual species condensate and use the inter-species FR between ^{87}Rb and ^{39}K to investigate the polaron, see figure 3.17. However a much wider intra-species FR was predicted between the two ^{39}K spin state, $|1\rangle \equiv |1,-1\rangle$ and $|2\rangle \equiv |1,0\rangle$, close to the field at which the BECs are prepared, see figure 4.1, so the prospect of using these spin states as medium and impurity was explored.

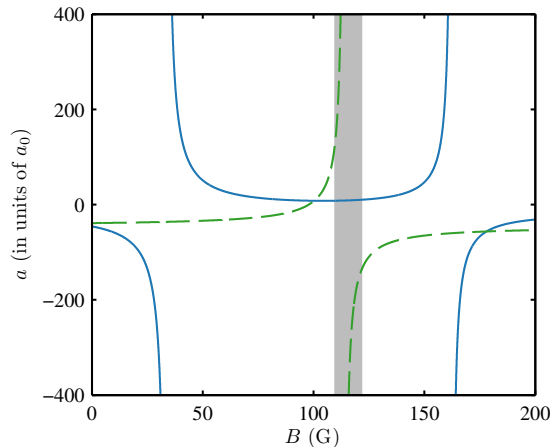


Figure 4.1: Intra-species FRs for ^{39}K . The scattering length between atoms in state $|1\rangle$ (blue solid line) is shown along with scattering length between atoms in $|1\rangle$ and $|2\rangle$ (green dashed line). The grayshaded region shows the region where the polaron experiment is performed.

All the ^{39}K atoms can then be prepared in the $|1\rangle$ and the polaron state can then be probed by spin flipping the atoms into the $|2\rangle$ state. This is illustrated in figure 4.2 where the $|1\rangle \rightarrow |2\rangle$ transition is driven by an RF pulse. The frequency of the pulse is scanned during the experiment and the repeated for different interaction strengths $\frac{1}{k_n a}$.

The preparation sequence described in the previous chapters is therefore altered as all of the rubidium is evaporated away in the QUIC trap. The experiments

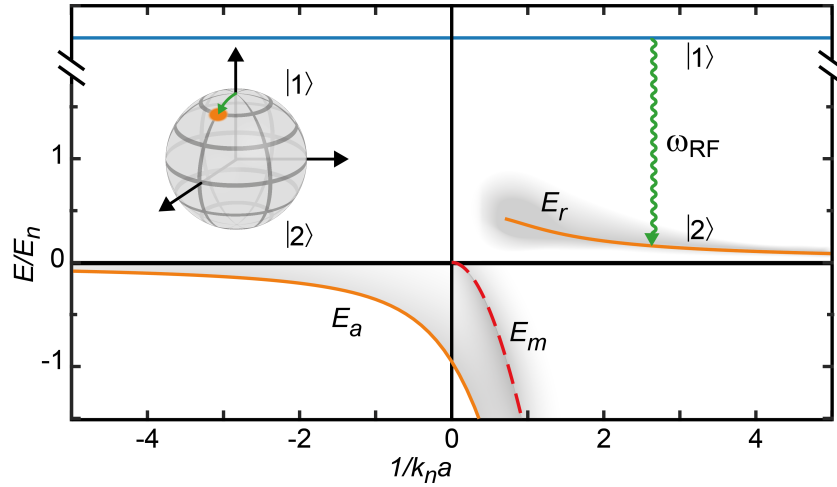


Figure 4.2: Sketch of the spectroscopic response from the RF pulse at different interaction strengths $\frac{1}{k_n a}$. The transition is driven from the $|1\rangle$ state (blue line) towards the $|2\rangle$ state (black vertical zero line) by the RF pulse (green wiggly line). As indicated by the inset this corresponds to a rotation of a small angle on the Bloch sphere. As the frequency of the pulse is scanned the many-body continuum of the states are probed, more on these states in section 2.4.

following will individually be performed in thermal clouds as well as BECs, these are prepared by evaporating down to 380 mW and 278 mW in the dipole trap, respectively. The thermal clouds allows us to probe the bare atomic transition of state $|2\rangle$ and the molecular band E_m . This is the same picture as figure 4.2 presents but without the polaron branches. This is important since it allows us to provide the two following key elements to the framework, which we use in the polaron experiment. First of all the magnetic field stability and calibration must be established. This is done in section 4.1 by probing the bare atomic transition in a thermal cloud. To employ the FR it must first be characterized. This has been done in section 4.2 utilizing a rethermalization measurement and measurements the molecular binding energy, also performed in a thermal cloud. Finally the measurement of the polaron spectroscopy has been carried out in section 4.3.1 and here the main result, the Bose polaron energy spectrum, is presented and discussed.

4.1 Magnetic field calibration

In the following experiments the magnetic field B is controlled and known with high precision. To achieve this, a B -field calibration is performed utilizing the hyperfine $|1\rangle \rightarrow |2\rangle$ transition frequency f . The experiment is performed in a thermal cloud, such that strong interaction effects does not arise with the high scattering lengths at the associated FR. The potassium is simply prepared in the

$|1\rangle$ state and the magnetic field is ramped to the desired value, followed by the RF pulse to the $|2\rangle$ state. The extraction of these transition energy positions will be described in detail in the following section. The hyperfine transition is driven for multiple magnetic fields and matched with the energy shift expected from the Zeeman effect, which is described by the Breit-Rabi formula:

$$\Delta E_{F=1,m_f} = -\frac{h\Delta W}{2(2 \cdot I + 1)} + \mu_B g_I m_F B - \frac{h\Delta W}{2} \sqrt{1 + \frac{2m_F x}{I + 1/2} + x^2},$$

where h is the Planck constant, ΔW is the splitting of the hyperfine states in the absence of a magnetic field, μ_B is the Bohr-magneton, I is the nuclear spin ($I = 3/2$ for ^{39}K), g_I is the gyromagnetic factor, m_F is the magnetic substate, $x \equiv \frac{\mu_B B (g_J - g_I)}{h\Delta W}$, and g_J is the Landé g-factor. The energy of the measured transition frequency corresponds to the energy difference arising when both energy levels are shifted, i.e. $\Delta f_{RF} h = \Delta E_{F=1,m_f=-1} - \Delta E_{F=1,m_f=0}$.

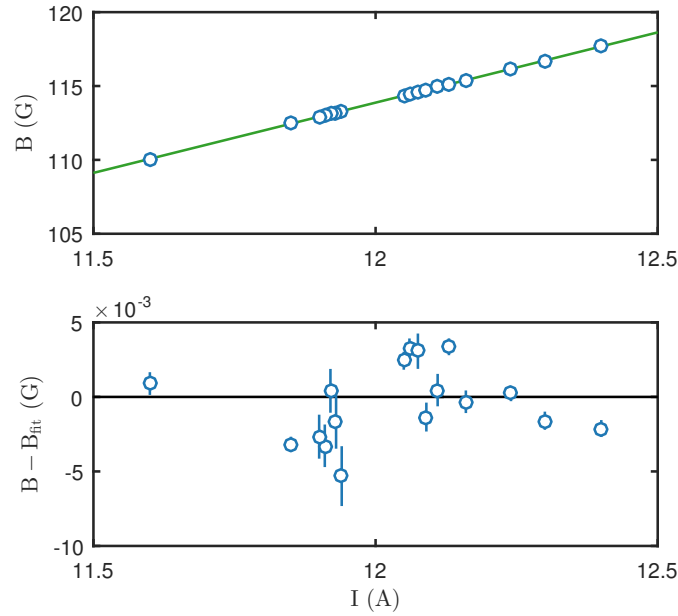


Figure 4.3: Magnetic field calibration. The magnetic fields (blue circles), extracted from the $|1\rangle \rightarrow |2\rangle$ transition frequencies, are shown as a function of current (top row). These are fitted with linear regression (green line) for which the residues have been plotted (lower row).

The transition frequencies were measured in a range of magnetic fields and as seen on figure 4.3 the data is well described by a linear fit. The residues shows that an uncertainty on the magnetic field below 5 mG is expected. It was suspected that the FR might influence the magnetic field calibration around its position 113.78 G, and the data might indicate that this is the case, but since it is below 5 mG and

probably within the noise, this should not pose a problem. The magnetic field response to the current I is:

$$B = 9.511 \text{ G A}^{-1} I - 0.259 \text{ G}$$

The offset indicates that there is an external magnetic field present and this is of the order of the earth's magnetic field. A conservative uncertainty is estimated from the residues to be about 5 G, which is more than enough for the purposes of this thesis.

4.2 Characterizing the inter-state Feshbach Resonance

To determine the scattering length between the atoms in state $|1\rangle$ and $|2\rangle$ the interstate FR needs to be characterized. This is done by exploiting two different consequences arising from the FR. First that the zero crossing of the FR can be determined by observing the rethermalization between the two components ($|1\rangle$ and $|2\rangle$). Since the rethermalization between the two species strongly depend on their mutual scattering length the position of zero crossing B_C can be revealed by cooling on one species and observe the temperature of the other. Then the position in magnetic field of peak temperature reflects the position of least interaction between the two species, i.e. the zero crossing, see figure 4.4.

The experiment is performed by preparing both spin components in the dipole trap then, using the Ioffe-coil, part of the $|2\rangle$ state is pushed out of the trap, i.e. is evaporatively cooled. Note that it is the gradient of the Zeeman effect around 100 G that leads to a force on the atoms, see figure 4.5a, and therefore the $|2\rangle$ state is pushed out of the trap rather than the $|1\rangle$ state. Afterwards the Ioffe-coil is turned off and the magnetic field is ramped to the appropriate field for which rethermalization is investigated. By doing so the two components are prepared with the same temperature difference each time.

The rethermalization between the two components assume an exponential decay in temperature with respect to the two-body scattering process $e^{-\beta a^2}$. The scattering length close to resonance is approximate given by [5]:

$$a = a_{bg} \left(1 + \frac{\Delta}{B - B_0} \right) = a_{bg} \left(1 + \frac{B_0 - B_C}{B - B_0} \right). \quad (4.2.1)$$

So to determine the zero crossing a function on the following form is fitted to the data

$$\Delta T = \Delta T_0 e^{-\tilde{\beta} \left(1 + \frac{B_0 - B_C}{B - B_0} \right)^2},$$

where B_C is the free parameter to the fit along with $\tilde{\beta}$, a parameter containing a_{bg} that makes the exponent dimensionless. The resonance position B_0 is set to

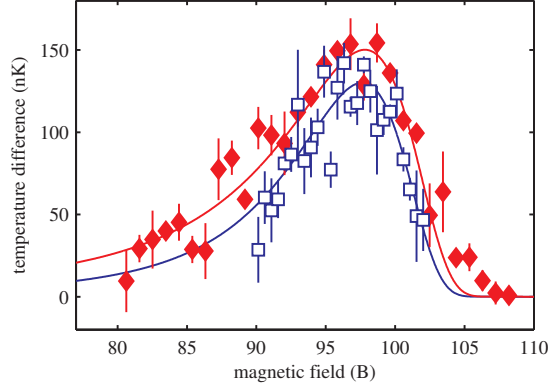


Figure 4.4: Temperature of $|1\rangle$ as a function of magnetic field for a hold time of 5 s (red diamonds) and 10 s (blue squares).

a static value of 113.8 G, there is not a particular dependence of this parameter in the regime we are fitting to so this suffice to determine the zero crossing. This yields a value of $B_C = 97.9$ G.

To determine a_{bg} and B_C we exploit that the molecular binding energy is related to the scattering length by eq. (2.2.1) (with the range parameter being about $60 a_0$). By using this formula the scattering lengths at different magnetic fields can be extracted by measuring the molecular binding energy. The molecular state is formed just beneath the $|2\rangle$, as seen on the inset of figure 4.5a, and are observed through the a RF spectroscopy which reveals two peaks, one bare atomic state followed by the molecular state, see figure 4.5b. Note that energy of the molecular state lies lower on absolute scale, but we are driving the state from $|1\rangle$ *down* to either the bare atomic state or the molecular state, and therefore the RF frequency is higher on figure 4.5b for the molecular band. As seen in the figure the state manifest themselves as dips in the number of atoms in state $|1\rangle$. It is convenient to detect the states this way, since the molecules are not detectable with the standard absorption imaging.

The positions of the two peaks are evaluated by applying a function containing two Gaussian distributions to each of the transitions. This is illustrated in figure 4.6. The energy position for the bare transition can the be extracted from the energetically lower lying Gaussian function, and similarly the molecular energy position from the energetically higher lying.

The extracted scattering length as function of the B -field is shown in figure 4.7. These are fitted with a function of type eq. (4.2.1), with B_C kept at the value extracted from the rethermalization experiment. The resulting parameters final parameters extracted are; $B_0 = 113.78$ G, $\Delta B = -15.88$ G and $a_{bg} = -45.34 a_0$.

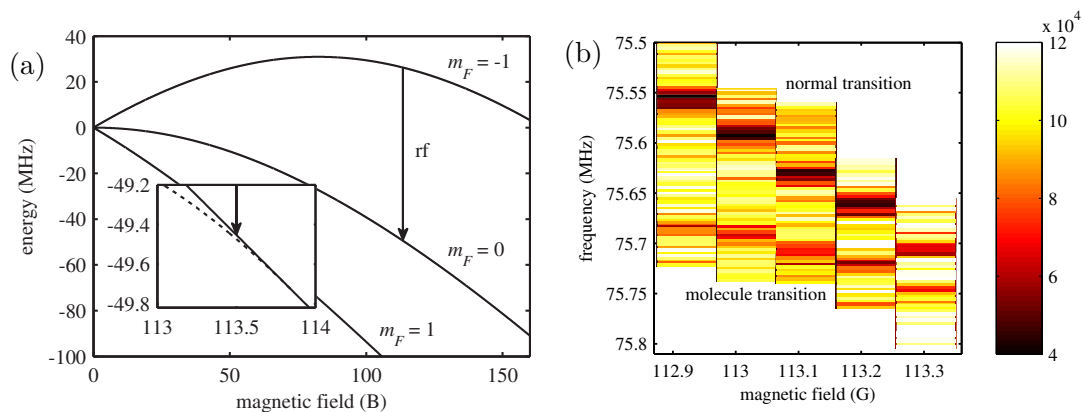


Figure 4.5: Interstate FR spectroscopic response Adapted from [10].

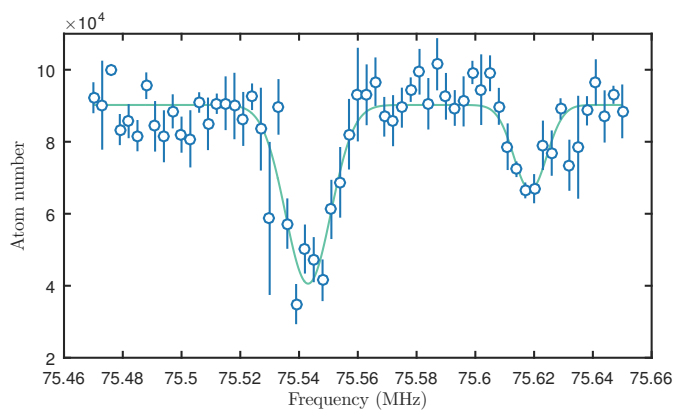


Figure 4.6: Spectra for a thermal cloud $|1\rangle$ state using the number of atoms (blue circles) and fit of a double Gaussian function (green line). Left signal arising from the bare atomic state and right signal from the molecular state.

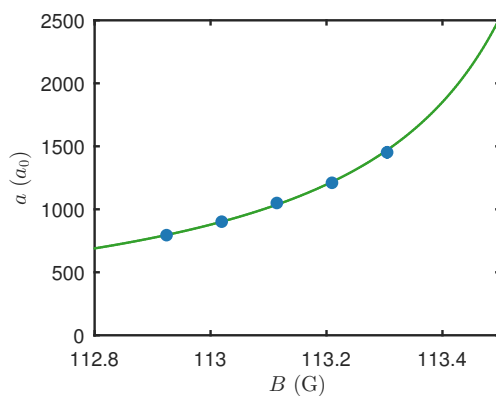


Figure 4.7: Scattering length values as function of magnetic field (blue dots). A FR fit (green line) of the type eq. (4.2.1) is fitted to the scattering lengths extracted from the molecular energy.

4.3 Polaron spectroscopy

The Bosonic polaron is measured by preparing the ^{39}K BEC in a weakly interacting state, $|1\rangle$. Then the 10 % of the atoms is spin-flipped to the strongly interacting $|2\rangle$ state. This is done by irradiating the sample for 100 μs RF pulse. The scattering length is controlled through the intra species FR. It is this same spin flip for which the RF frequency is varied. By probing the flip with a short pulse, the spectrum can be expected to reflect the spectral function of the impurity interacting with the BEC medium. In the following sections I might refer to the Bose polaron simply by the polaron.

Because the impurity is interacting strongly with the medium, three-body recombination will occur involving one $|2\rangle$ state atom and two $|1\rangle$ state atoms. Therefore the spectrum of the wave function describing the polaron (an impurity interacting with a medium) is reflected in the loss in atom number for the frequency scan. There is a trade off here, since a stronger signal can be achieved by increasing the power, but since we still want to be in a regime where the polaron is well described, a major number of medium atoms must be present. For this an order of magnitude between the number of impurity and medium atoms are chosen leading to a restriction on the loss of about a third, which correspond to one impurity atoms per nine medium atom.

A typical spectrum is shown in figure 4.8. To the two spectra a Gaussian function of the form

$$N(E) = N_0 - N_p e^{-\frac{(E_p - E_0)^2}{2\sigma^2}},$$

has been fitted. Here N_0 is the initial number of atoms (referred to as the background atom number), N_p is the signal peak atom number, i.e. the number of atoms lost at the peak, E_0 is the resonance energy, σ is the signal width, and E_p is the energy variable of the spectrum.

The average density of the BEC can be calculated, using the Thomas-Fermi approximation

$$\bar{n} = \int dV \left\{ \frac{n(\mathbf{r})^2}{N_0} \right\} = \frac{15}{14\pi} \frac{N_0}{r_x r_y r_z},$$

where \mathbf{r} is the radius vector, V is the volume, $r_i = \frac{2\mu}{m_K \omega_i^2}$, μ is the chemical potential for the medium BEC, ω_i is the trap angular frequency in direction i , and m_K is the ^{39}K mass. The average density is used when calculating the interaction strength $\frac{1}{k_n a}$ of the signal. By doing so, the small fluctuations in density is corrected for through $k_n = (6\pi^2 n)^{1/3}$ when comparing spectra at different interaction strengths.

Because the density of a thermal cloud is about two orders of magnitude lower than that of a BEC cloud, performing the spectroscopy in the thermal cloud makes it possible to probe the bare (or unperturbed) atomic transition at a similar scattering length, see figure 4.8. The signal provided by the thermal cloud then matches

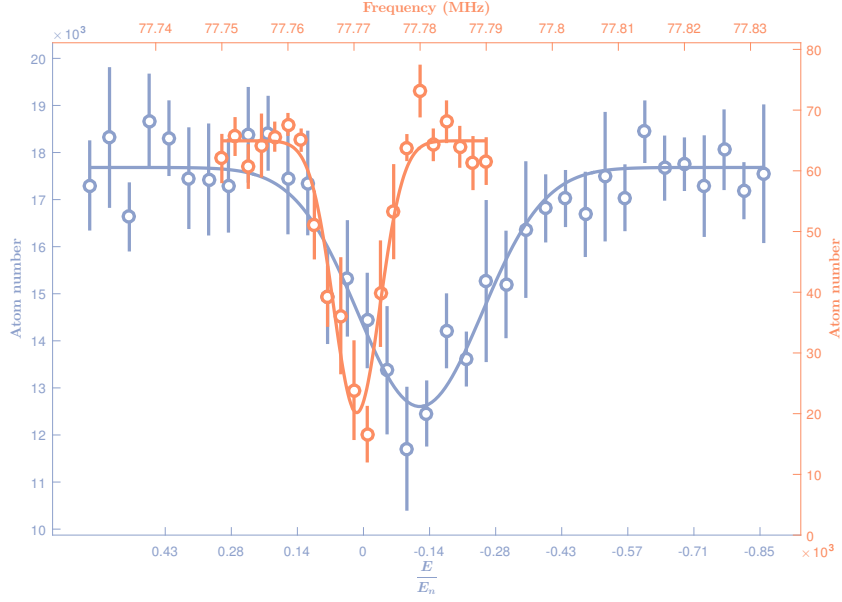


Figure 4.8: Spectrum of the thermal cloud (orange) and the BEC cloud (blue) at $\frac{1}{k_n a} = -1.6$. The x-axis of the BEC scan is conveniently shifted with respect to the bare atomic transition.

a probing of the bare transition. Whereas the signal from the BEC will provide a measurement of the perturbed polaron state.

For convenience the energy scale in figure 4.8 has been shifted with respect to the unperturbed transition energy, such that the relative energy shift due to the polaron state can be read out on the x-axis.

In theory, the spectral line shape of the polaron is unique at each value of $\frac{1}{k_n a}$, but a Gaussian function fit well throughout the range of interactions for evaluation.

To make the spectrum more convenient to compare with other spectra, each spectrum was individually scaled after the fit was performed

$$N(E) \rightarrow -\frac{N(E) - N_0}{N_p}.$$

This first shifts the atom number down by the background, N_0 , secondly each spectrum is normalized such that it has a peak corresponds to one. Note that this normalization leads to negative values and values above one, due to shot-to-shot atom number fluctuations. Finally the minus sign simply mirrors the signal in the energy axis, such that the signal is positive.

4.3.1 Energy spectrum

To map out the polaron energy in response to different scattering length the energy spectra were recored around the FR. The measured data is shown in figure 4.9a

along with the theoretically predicted spectroscopic responses in figure 4.9b. The theoretical spectrum is scaled such that the frequency integrated weight is the same at each interaction strength.

As seen on figure 4.9a there are two polaron branches. On the attractive side a polaron branch is created at lower energies and on the repulsive side a polaron branch is created at higher energies. As they approach the FR from their respective sides they both diverge away from the bare transition ($\frac{\hbar\Delta}{E_n} = 0$). The molecular branch has also been accounted for in the TBM calculation where, in the absence of noise, it is clear how it merges the two branches together.

On panels 4.9c to 4.9g the data of individual spectra at different $\frac{1}{k_n a}$ are shown along with their theoretical curves calculated with TBM, one taking the three-body correlations into account and one that does not take three-body correlations into account). Comparing the two, it is clear that three-body correlations does not have a significant influence in the mean-field regime.

When moving closer to resonance from the attractive side ($\frac{1}{k_n a} = -0.62$) a tiny tail is formed towards higher energies due to the *grass* and broadening occur, but for the theory that takes three-body correlations into account the broadening is much more significant and it is clear that the data is better described including this effect. When comparing close to unitarity ($\frac{1}{k_n a} = -0.04$) the extra hump on the red dashed line is due to the resonance of the molecular band, this band is significantly distorted when taking three-body correlations into account, but it is clearly necessary to get a good description of the data.

Moving to the repulsive regime ($\frac{1}{k_n a} = 1.6$) the theory both with and without the three-body correlations is less successful, this is breakdown of the theory is probably caused by coupling to the additional energy levels below the repulsive branch, due to the molecular band, which leads to complications of the theory which are difficult to account for. In the mean-field regime ($\frac{1}{k_n a} = 4.39$) the three-body correlations again does not have any effect on the shape and the data is adequately described by either.

From a qualitative view there is a strong resemblance between the measured polaron energy and the theoretical values. To make a more quantitative comparison the peak position and variance was extracted by applying Gaussian function fits, see section 4.3, to both the measured and calculated spectra.

4.3.2 Energy

Three main parts form the observed polaron spectra; the Fourier width of the square RF pulse, the polaron energy position and the inhomogeneity of the BEC density. The first puts a minimum on the width, of about $\sigma_\Delta \simeq 0.064 E_n$, which can be observed in the mean-field regime. The result of the convolution with the inhomogeneous density will be a peak position near the most populated density, which for the Thomas-Fermi distribution is a bit higher than the average density

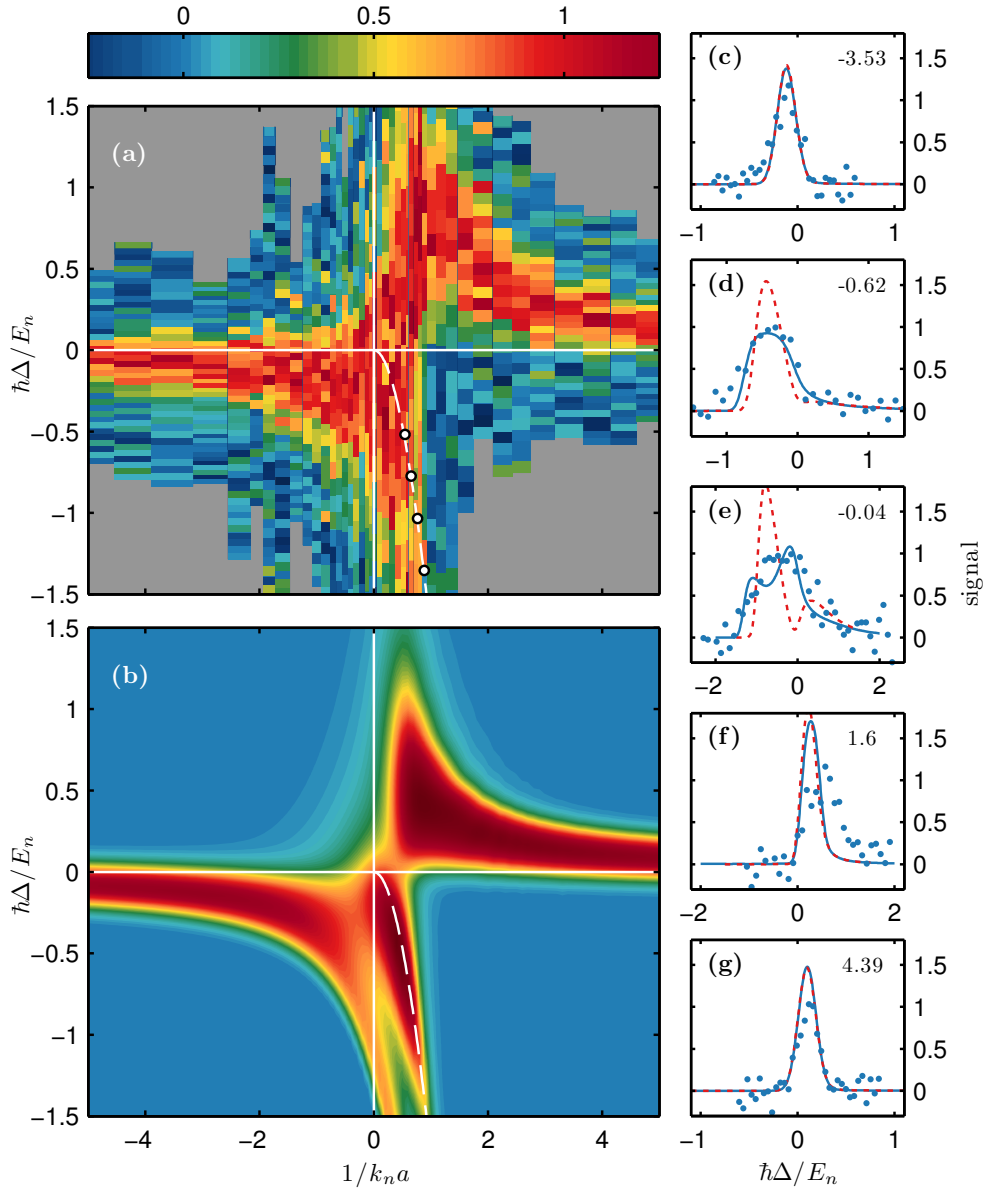


Figure 4.9: Contours of the Bose polaron energy spectra. The false color map shows the normalized signal at different detunings energies Δ and inverse gas parameters $\frac{1}{k_n a}$ for (a) the measured data and (b) the theory, calculated by the TBM. Additionally, the molecular transition, used to measure the scattering length is included (white dots) along with the fitted curve (white dashed line). Panels (c)-(g) shows the data (blue dots) for individual spectra at different $\frac{1}{k_n a}$ (right corner of panel), the theoretical curve (red dashed line) excluding three-body correlations, and the complete theoretical curve (blue solid line) including three-body correlations.

position.

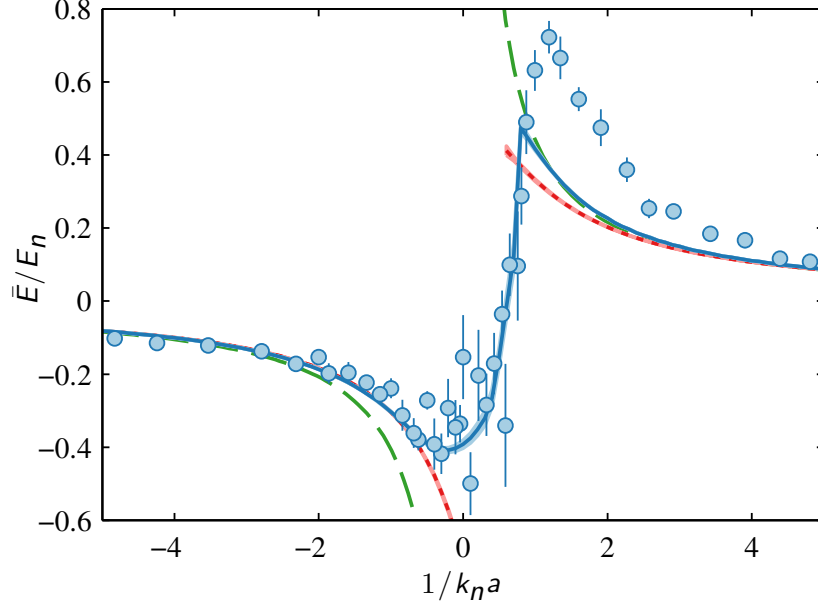


Figure 4.10: Resonance energy position of the polaron. The position of the energy extracted from the Gaussian fits (blue dots) along with different theories relevant for the experiment. The perturbation theory (green dashed line), the TBM without three-body correlations (red dotted line) and the TBM with three-body correlations (blue solid line). The shadings on the theory lines reflects a uncertainty of one standard deviation.

The energy positions extracted from the Gaussian fits are shown on figure 4.10, to make the theoretical values comparable Gaussian fits were applied to all theoretical contours. All theories reproduce the energy perfectly for weak interaction. For the repulsive polaron the theories all fail when going just beyond the weakly interacting regime, which is probably because of the aforementioned complications due to lower lying energy states. For the attractive polaron the story is quite different. Here the perturbation theory suffices beyond the weakly interacting regime, until $\frac{1}{k_n a} = -2$, moving into the strongly interacting regime the TBM without three-body correlations suffices to about $\frac{1}{k_n a} = -0.5$ but fails to reproduce the change in curvature towards positive energies, whereas the TBM with three-body correlations reproduces the curvature very well in the strongly interacting regime and into the shared region of the attractive and repulsive polaron.

4.3.3 Energy width

As for the energy position, the width of the energy is extracted from the Gaussian fits and has been plotted on figure 4.11. It is clear the variance converge towards a constant width that is close to that of the Fourier width of the square pulse. Again

the theories fail to reproduce the data on the repulsive side. The perturbation theory only reproduce part of the data for the attractive polaron in the semi-strongly interlacing regime ($-2.5 < \frac{1}{k_n a} < -0.5$). Comparing the two TBM methods it is clear that the broadening effect of the three-body correlations is necessary to reproduce the width, which it does well within a order of magnitude.

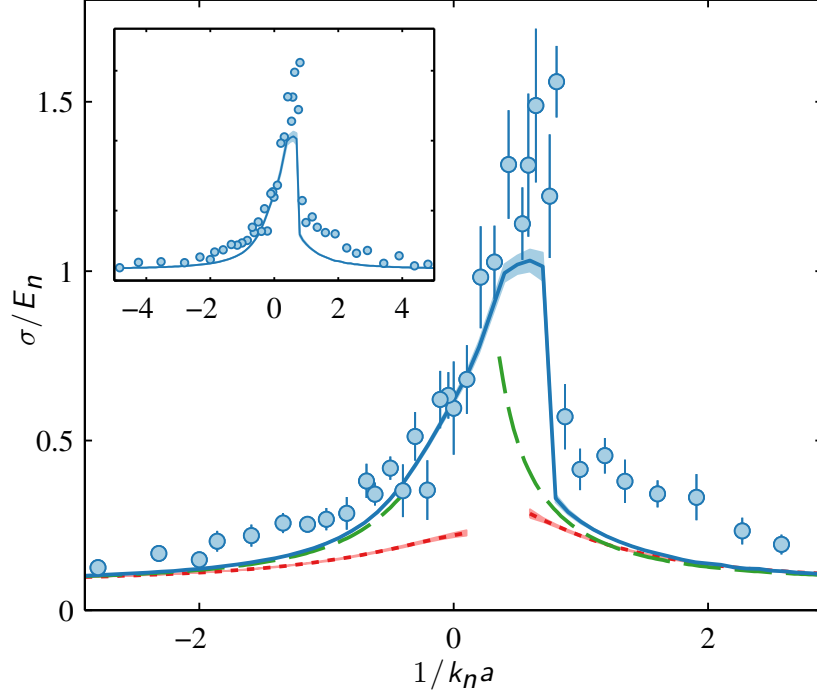


Figure 4.11: Variance of the polaron energy. The perturbation theory (green dashed line), the TBM without three-body correlations (red dotted line) and the TBM with three-body correlations (blue solid line). The shadings on the theory lines reflects a uncertainty of one standard deviation. The inset shows all data recorded and the three-body correlation TBM.

It was expected that three-body recombination would limit the lifetime of the polaron, which would be reflected in a broadening proportional to a^4 about unitarity, but as seen on figure 4.11 this can be disregarded. Therefore we interpret the polaron as long-lived or well-defined.

4.3.4 Power dependence

During the experiment we experienced that the response of the system with respect to the RF power was non-linear. To keep the pulse duration consistent the power was consequently tuned through the experiment to match the ratio $\frac{|N_p|}{N_0} \simeq \frac{3}{10}$. The resulting power is seen in figure 4.12, expressed in electric E field to make it comparable with the dimensions of the Rabi frequency.

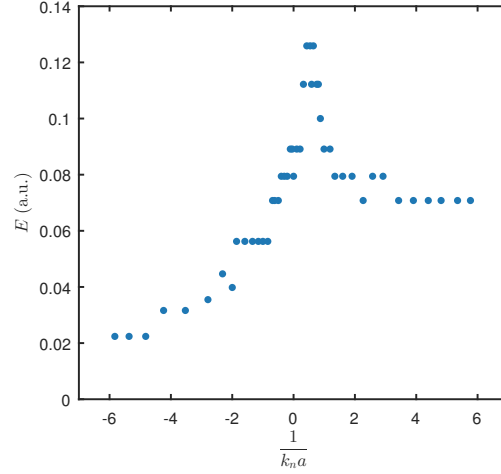


Figure 4.12: Power to keep system at $\frac{|N_p|}{N_0} \simeq \frac{3}{10}$.

As seen there is a slope present in the response from the weakly interacting attractive side to the weakly interacting repulsive side. This could originate from a non-constant scaling through the RF amplification system. Additionally the peak close to unitarity suggests a change in the Rabi frequency, due to the quasiparticle residue Z as expected from theory. In the experiment with the Fermi polaron a scaling to the Rabi frequency of about two is observed from the weakly interacting regime to unitarity. Here the observed scaling is a factor of about two to seven, depending on whether the repulsive or attractive side is chosen as reference, respectively.

4.3.5 Concentration dependence

The sensitivity of the concentration of impurities in the mixture were investigated by varying the RF power. The dependence was studied at multiple powers far below to far above the proper power setting. This was done at different $\frac{1}{k_n a}$ in both the strongly interacting attractive regime and the semi strongly interacting repulsive regime, see figure 4.13. Note that only the $N(E) \rightarrow \frac{N(E)}{N_p}$ transformation has been performed.

The Gaussian function fits well with the data for all the powers in the strongly interacting attractive regime, whereas it is less successful for high RF powers in the strongly interacting repulsive regime. As seen in the figure 4.13, the data curve for the repulsive regime at high RF powers becomes asymmetric compared to the Gaussian fit. The curve has a steep slope at lower energies and a tail formed towards higher energies. Part of the explanation for the formation of the tail towards higher energies is the many-body continuum, but besides this, the response of the system at the highest powers are not well-known either since the presumption of many more medium atoms compared to impurity atoms is false

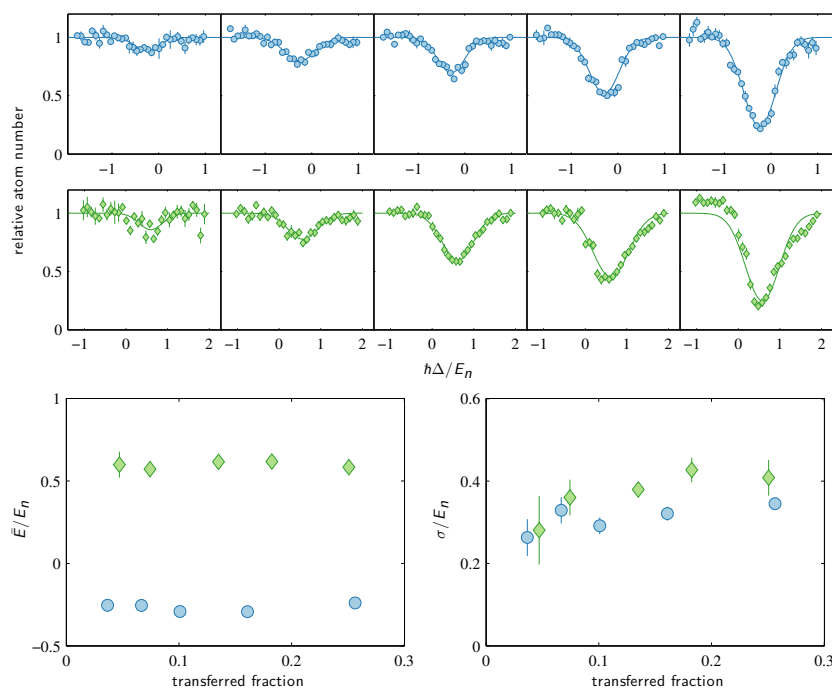


Figure 4.13: Polaron spectrum for multiple pulse strengths (top panels). Measured for $\frac{1}{k_n a} = -0.84$ (blue circles) and $\frac{1}{k_n a} = 1.6$ (green diamonds). The energy position (bottom left) and width (bottom right) are shown as a function of the transferred fraction.

and the description of the polaron breaks down.

Figure 4.13b shows the resonance position value and variance values of the Gaussian fits from figure 4.13. It is clear that the resonance position does not change dramatically as the power is changed. The highest power position value for the repulsive polaron might be different because of the bad fit mentioned earlier, but all spectra was recorded well below this transferred fraction $N_{|2\rangle}/N_{|1\rangle} \simeq \frac{1}{4}$, which corresponds to a ratio of about $|N_p|/N_0 \simeq \frac{3}{4}$.

The variance of the resonance is growing with the power, as should be expected, but seems to vary only about $0.1E_n$ with even very high transfer fractions. As indicated the by the error bar, the last data point for the repulsive polaron becomes more unreliable.

Conclusion and Outlook

The main result within this thesis is the first observation of the Bose polaron in an ultracold gas, made by employing RF spectroscopy and a FR between the $|1,-1\rangle$ and $|1,0\rangle$ spin states in ^{39}K . Note that this discovery was made in parallel with similar work of [25].

At the beginning of my work, late August 2015, I started with the build up of the characterization system for RADIANTDYES lasers. While finishing this I got familiar with the lab and the control system, as I got involved with the collection of the data for the FR characterization. For this I developed data evaluation scripts for the B -field calibration and molecular spectroscopy. The experimental routine was optimized for the highest ^{39}K PSD and atom number in the dipole trap in preparation of the polaron experiment. This was carried out in collaboration with Nils B. Jørgensen. At the start of 2016 I had gotten as familiar as to be able to run the experiment myself and correct basic errors. At this time the main goal was the collection and evaluation of the polaron data. For this, parts of the software architecture for the FR characterization was extended to an automated evaluation of the polaron data. This enabled us to study the contour of the polaron continuously while obtaining the data. To arrive at the final data evaluation many different ideas and evaluation techniques were explored. Late February I went to the Young Atomic Physicist (YAO) conference for a week to present our preliminary results on the polaron, see poster in appendix A. While working on maintenance of the experiment with Nils B. Jørgensen and Dr. Lars J. Wacker, the last polaron data was collected and the evaluation was finished during the last months before writing this thesis.

For comparison with the evaluated polaron data the thesis presents the prediction from both the perturbational and variational method. The spectroscopic response of the polaron was predicted using a perturbation and variational method. The perturbation theory predicts the energy of the weakly interacting polaron well, but evidently fails for stronger interactions. The variational method that takes three-body correlations into account reproduces the energy contour with stunning resemblance. However both theories have trouble replicating the spectroscopic response of the repulsive polaron. This is because theory breaks down due to the presence of lower lying states, provided by the molecular and attractive polaron

bands, which the repulsive polaron can decay into complicating the theory. As the spectroscopic response of the polaron is described by the theory without broadening effects arising from three body recombination, the polaron is characterized as well-defined.

Since the intra-species FR was used to control the interaction between the two spin states, a byproduct of the thesis was the investigation of this resonance. It was successfully conducted by exploring the magnetic dependence of the rethermalization, identifying the zero-crossing, and molecular binding energy. By inclusion of both the FR was characterized by the parameter values; $B_0 = 113.78 \text{ G}$, $\Delta B = -15.88 \text{ G}$ and $a_{bg} = -45.34 a_0$.

The discovery of the Bose polaron leads to a whole branch of properties that can be investigated with this system, such as the quasiparticle residue, how the polaron behaves under a phase transition, such as melting a BEC, its dynamics and its interaction with other polarons.

In the near future the two major upgrades will be implemented in the lab. One is the Faraday imaging system, which is a non-destructive imaging technique relying on the polarization the light when propagating through the cloud [26]. This will strongly enhance the data for our evaluation of the clouds and with the improvements on the evaluation software, also under development, our data quality for the coming experiments will significantly improve. Secondly an additional 806 nm laser has been installed to compensate for the gravitational force on the two species. This influences the atoms in the same manner as the ODT (far detuned from transition), and by tuning of frequency and power it should be possible to compensate for the difference in mass, thereby trapping the atoms in a potential that is countering gravity.


With these improvements the properties of the polarons can be explored along with many other experiments with strongly interacting ultracold mixtures.

Bibliography

- [1] Mike H Anderson, Jason R Ensher, Michael R Matthews, Carl E Wieman, and Eric A Cornell. Observation of Bose-Einstein condensation in a dilute atomic vapor. *science*, 269(5221):198–201, 1995.
- [2] C. Kohstall, M. Zaccanti, M. Jag, A. Trenkwalder, P. Massignan, G. M. Bruun, F. Schreck, and R. Grimm. Metastability and coherence of repulsive polarons in a strongly interacting Fermi mixture. *Nature*, 485:615–618, 2012.
- [3] André Schirotzek, Cheng-Hsun Wu, Ariel Sommer, and Martin W. Zwierlein. Observation of Fermi Polarons in a Tunable Fermi Liquid of Ultracold Atoms. *Phys. Rev. Lett.*, 102:230402, 2009.
- [4] Marco Koschorreck, Daniel Pertot, Enrico Vogt, Bernd Frohlich, Michael Feld, and Michael Kohl. Attractive and repulsive Fermi polarons in two dimensions. *Nature*, 485:619–622, 2012.
- [5] Cheng Chin, Rudolf Grimm, Paul Julienne, and Eite Tiesinga. Feshbach resonances in ultracold gases. *Rev. Mod. Phys.*, 82:1225–1286, 2010.
- [6] L. Wacker, N. B. Jørgensen, D. Birkmose, R. Horchani, W. Ertmer, C. Klempt, N. Winter, J. Sherson, and J. J. Arlt. Tunable dual-species Bose-Einstein condensates of ^{39}K and ^{87}Rb . *Phys. Rev. A*, 92:053602, 2015.
- [7] Nils B. Jørgensen, Lars Wacker, Kristoffer T. Skalmstang, Meera M. Parish, Jesper Levinsen, Rasmus S. Christensen, Georg M. Bruun, and Jan J. Arlt. Observation of attractive and repulsive polarons in a Bose-Einstein condensate. To be published in Physical Review Letters 29/07-2016.
- [8] L. Landau. Electron Motion In crystal Lattices. *Phys. Z. Sovjet*, 664:1, 1933.
- [9] C. J. Pethick and H. Smith. *Bose-Einstein condensation in dilute gasses*. University Press, Cambridge, second edition, 2008. ISBN 978-0-521-84651-6.
- [10] Nils Byg. Few-body physics in ultracold mixtures of potassium and rubidium, progress report, 2015.

-
- [11] Rasmus Søggaard Christensen, Jesper Levinsen, and Georg M. Bruun. Quasi-particle Properties of a Mobile Impurity in a Bose-Einstein Condensate. *Phys. Rev. Lett.*, 115:160401, 2015.
- [12] Jesper Levinsen, Meera M. Parish, and Georg M. Bruun. Impurity in a Bose-Einstein Condensate and the Efimov Effect. *Phys. Rev. Lett.*, 115:125302, 2015.
- [13] M. Cetina, M. Jag, R. S. Lous, I. Fritsche, J. T. M. Walraven, R. Grimm, J. Levinsen, M. M. Parish, Schmidt R., M. Knap, and E. Demler. Ultrafast many-body interferometry of impurities coupled to a Fermi sea. arXiv:1406.6506, 2016.
- [14] Lars Wacker. *Few-body physics with ultracold potassium rubidium mixtures*. PhD thesis, Aarhus University, 2015.
- [15] Danny Matthiesen Birkmose. *Investigation of Dual Species Bose-Einstein Condensates*. PhD thesis, Aarhus University, 2015.
- [16] Nils Winter. *Creation of ^{39}K Bose-Einstein Condensates with tubable interactions*. PhD thesis, Aarhus University, 2013.
- [17] C. Klempt, T. van Zoest, T. Henninger, O. Topic, E. Rasel, W. Ertmer, and J. Arlt. Ultraviolet light-induced atom desorption for large rubidium and potassium magneto-optical traps. *Phys. Rev. A*, 73:013410, 2006.
- [18] B. H. Brandsen and C. J. Joachain. *Physics of Atoms and Molecules*. Pearson Education Limited, second edition, 2003. ISBN 978-0-582-35692-4.
- [19] X. Baillard, A. Gauguet, S. Bize, P. Lemonde, Ph. Laurent, A. Clairon, and P. Rosenbusch. Interference-filter-stabilized external-cavity diode lasers. *Optics Communications*, 266(2):609 – 613, 2006. ISSN 0030-4018.
- [20] T. G. Tiecke. Properties of Potassium. unpublished, 2011.
- [21] L Mudarikwa, K Pahwa, and J Goldwin. Sub-Doppler modulation spectroscopy of potassium for laser stabilization. *Journal of Physics B: Atomic, Molecular and Optical Physics*, 45(6):065002, 2012.
- [22] K. Pahwa, L. Mudarikwa, and J. Goldwin. Polarization spectroscopy and magnetically-induced dichroism of the potassium D2 lines. *Opt. Express*, 20(16):17456–17466, 2012.
- [23] R. Grimm, M. Weidemüller, and Y. B. Ovchinnikov. Optical dipole traps for neutral atoms. *Advances in atomic, molecular, and optical physics*, 42: 95–170, 2000.

-
- [24] G. Reinaudi, T. Lahaye, Z. Wang, and D. Guéry-Odelin. Strong saturation absorption imaging of dense clouds of ultracold atoms. *Optics letters*, 32(21):3143–3145, 2007. ISSN 0146-9592.
- [25] Ming-Guang Hu, Michael J. Van de Graff, Dhruv Kedar, John P. Corson, Eric A. Cornell, and Deborah S. Jin. Bose polarons in the strongly interacting regime. Soon to be published in *Physical Review Letters*, 2016.
- [26] Miroslav Gajdacz, Poul L. Pedersen, Troels Mørch, Andrew J. Hilliard, Jan Arlt, and Jacob F. Sherson. Non-destructive Faraday imaging of dynamically controlled ultracold atoms. *Review of Scientific Instruments*, 84(8):083105, 2013.




**AARHUS
UNIVERSITET**

Toward the Bose Polaron in an ultracold gas

Kristoffer T. Skalmstang, Nils B. Jørgensen,
Lars Wacker, Georg Bruun and Jan Arlt

Danish National Research Foundation Center for Quantum Optics - QUANTOP
Department of Physics and Astronomy, Aarhus University, Ny Munkegade 120, 8000 Aarhus C, Denmark



Abstract

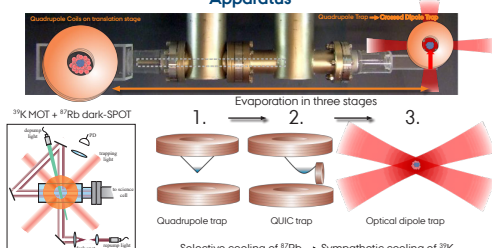
We present the production of dual-species Bose-Einstein condensates of ^{39}K and ^{85}Rb by employing sympathetic cooling of ^{39}K with ^{85}Rb . By preparing both species in the $|F=1, m_f=-1\rangle$ state we were able to exploit a total of three Feshbach resonances enabling simultaneous tuning of the ^{39}K - ^{85}Rb interspecies scattering length. This allowed for dual-species condensates with tunable interactions for which, the miscible to immiscible phase transition, could be investigated [1].

An impurity interacting with its surroundings leads to the formation of a quasi particle, called a polaron. In 1933 Landau first described the polaron, formed in a solid by the interaction between the electron and the lattice displacements, described as a bosonic phonon gas. Ultracold gases, with their high degree of control, are a perfect test bench to study such impurity systems. The first experimental investigations of the Fermi polaron have already been achieved in mixtures of ultracold Fermi gases [2].

Likewise, bosonic polarons can be investigated using mixtures of ultracold bosonic gases. Here we present our study of the Bose polaron, where we employ a magnetic Feshbach resonance to tune the interaction between two spin states of ^{39}K . We record the energy spectrum of the impurity at different interaction strengths, allowing us to distinguish between the mean field energy regime and the appearance of the polaronic signature in the spectrum.

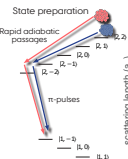
References:
[1] L. Wacker, N. B. Jørgensen, G. Bruun, K. Skalmstang, N. B. Jørgensen, C. Klemm, N. B. Jørgensen, and J. Arlt, *Phys. Rev. A* **92**, 033402 (2015)
[2] J. Edgar, S. Jochim, S. B. P. Rosenow, and P. Pellegrini, G. M. Bruun, F. Schreck and R. Grimm, *Nature* **465**, 655-658 (2012).

Apparatus



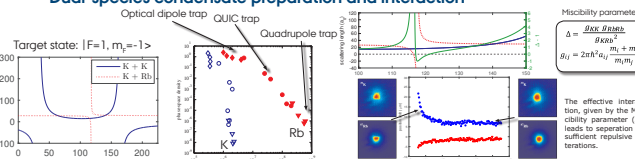
Selective cooling of $^{85}\text{Rb} \rightarrow$ Sympathetic cooling of ^{39}K

State preparation



Rapid adiabatic passages
 $|a, b\rangle$
 $|b, a\rangle$
 π -pulses

Dual-species condensate preparation and interaction



Target state: $|F=1, m_f=-1\rangle$

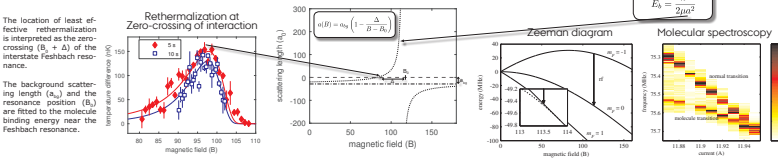
Miscibility parameter:
 $\Delta = \frac{4\pi\hbar^2 a_{ij} n_j}{m_i k_B T}$
 $g_{ij} = 2\pi\hbar^2 a_{ij} \frac{m_j}{m_i m_j}$

The effective interaction, given by the Miscibility parameter (Δ), leads to separation for sufficient repulsive interactions.

Characterizing an inter-state Feshbach Resonance in ^{39}K

The location of least effective rethermalization is interpreted as the zero-crossing ($B_0 = A_0$) of the inter-state Feshbach resonance.

The background scattering length (a_{ij}) and the resonance position (B_0) are fitted to the molecule binding energy near the Feshbach resonance.



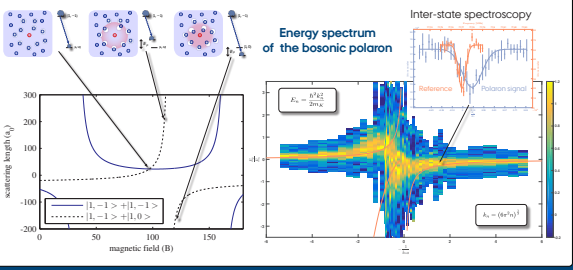
Rethermalization at Zero-crossing of interaction

Zeeman diagram

Molecular spectroscopy

$E_k = \frac{\hbar^2 k^2}{2m}$

Towards the Bosonic polaron



Energy spectrum of the bosonic polaron

Inter-state spectroscopy

$E_k = \frac{\hbar^2 k^2}{2m}$

$E_k = \hbar\omega + \epsilon(k)$

Outlook

- Implementation of a Faraday imaging system for non-destructive probing of ultracold samples and post selection of data
- Dual-species gravity compensation with a magic wavelength dipole trap
- Dynamics of dual-species condensates at various interspecies interactions
- Determining the polaron quasi-particle residue
- Search for the second triatomic Efimov resonance at multiple Feshbach resonances in ^{39}K